TAL TECH

SCHOOL OF SCIENCE

Distribution of Rare Earth Elements
in Estonian Lower Ordovician Complexes

Master thesis

Student: Henri Olavi Suomalainen

Student code: 204398LARM

Supervisor: Rutt Hints, PhD, Senior Researcher -

Head of the Division of Mineral Resources and Applied Geology: Department of Geology

Co-supervisor: Sophie Graul, MSc, Early Stage Researcher -

Division of Mineral Resources and Applied Geology: Department of Geology

Study programme: Georesources (LARM18/20)

Tallinn 2024

Haruldaste muldmetallide levik Eesti Alam-Ordoviitsiumi kivimkompleksides

Magistritöö

Üliõpilane: Henri Olavi Suomalainen
Üliõpilaskood: 204398LARM
Juhendaja: Rutt Hints, PhD, vanemteadur -
maavarade ja rakendusgeoloogia osakonna juhataja, geoloogia instituut
Kaasjuhendaja: Sophie Graul, MSc, doktorant-nooremteadur -
maavarade ja rakendusgeoloogia osakond, geoloogia instituut
Õppekava: maapõueressursid (LARM18/20)

Tallinn 2024

Declaration

I hereby declare that I have written this thesis independently and the thesis has not previously been submitted for defence. All works and major viewpoints of the other authors, data from sources of literature and elsewhere used for writing this paper have been properly cited.

Author: Henri Olavi Suomalainen

[Digitally signed]

The thesis complies with the requirements for master's theses.

Supervisor: Rutt Hints, PhD, Senior Researcher, Head of the Division of Mineral Resources and Applied Geology: Department of Geology

[Digitally signed]

Co-supervisor: Sophie Graul, MSc, Early Stage Researcher, Division of Mineral Resources and Applied Geology: Department of Geology

[Digitally signed]

Table of Contents

Distribution of Rare Earth Elements in Estonian Lower Ordovician Complexes

Abstract

The energy demand and need for mineral resources increases every day. A global shift to green energy alternatives has led to a need for rare earth elements (REEs), which could be potentially recovered also from Estonian sedimentary complexes. However, the scarcity of data on REE distribution limits the ability to assess these sources. The goal of the thesis is to provide systematic high-resolution information on REE variability in Estonian Lower Ordovician complexes using whole rock data from different lithologies (limestone, glauconitic sandstone, mudstone, and phosphorite).

The samples for the study were collected from borehole PH012B in Aseri, Estonia. Stratigraphically studied interval spans from the Toila Formation to the Kallavere Formation. Multi-instrumental (ICP-MS, XRF, and XRD) analyses were conducted on 117 samples using high-resolution sample sets to provide a comprehensive overview of REEs and related chemical and mineralogical variables.

According to the results, total REE content for limestones is on average 95±2 ppm, for glauconitic sandstones 142±2 ppm, for mudstones 157±6 ppm, and for phosphorites 1026±23 ppm. The average sum of LREE (La, Ce, Pr, Nd) in all the complexes is 929.23 ppm, the sum of MREE (Sm, Eu, Gd, Tb, Dy) is 161.07 ppm, and the sum of HREE (Ho, Er, Tm, Yb, Lu) is 51.54 ppm. The PAAS normalised REE patterns suggest that the enrichment levels of the complexes are similar to that of average shale. However, for phosphorite, some REEs show up to ten-fold enrichment. Despite the varying enrichment levels, a common feature is the MREE enrichment. Ce, Eu, Y anomalies were detected in various complexes. For limestones, it can be concluded that calcite formation did not have a major control on REE accumulation in primary sediments and that the measured REE signal is likely partially inherited from terrigenous fraction. In glauconitic sandstones a strong positive correlation between apatite and REEs is observed, suggesting that REE capture is most likely connected to apatite. In mudstones, considering that the REE enrichment is statistically related to quartz and apatite contents, the latter being likely the main carrier phase of REEs. Phosphorite has the strongest correlation of REEs with other compounds, apatite, dolomites, and MnO. The enrichment of MREE relative to LREE and HREE suggests a preferential uptake and fractionation relative to seawater, likely by stagewise sequestration pathways, as suggested by recent studies.

Different elemental ratios were studied to gain information about the prevailing redox conditions and primary sources of REE. Based on Ce anomaly calculations, only shelly phosphorite samples fell into the 'anoxic' field, while all the other samples produced 'suboxic' signatures. Furthermore Y/Ho ratios of studied lithologies prevailingly produced a 'terrigenous input' signal, except for the phosphorite samples, most of which demonstrate more seawater-like signatures. Recorded irregular Eu/Eu* signals for limestone and mudstone might indicate Ba interferences with Eu signals during ICP-MS. Nevertheless, this might also indicate a potential hydrothermal influence or Mn and Fe cycling in diagenetic environments. The obtained data provide good basis for further in-depth studies both from paleoenvironmental and resource perspectives.

Haruldaste muldmetallide levik Eesti Alam-Ordoviitsiumi kivimkompleksides

Annotatsioon

Vajadus mineraalsete toormete ja energia järele kasvab iga päevaga. Üleminek rohelistele energiatehnoloogiatele on suurendanud veelgi enam vajadust tänapäeval laialdast kasutust leidvate haruldaste muldmetallide (HMM) järele. Potentsiaalselt saaks neid ammutada ka Eesti enda settekivimitest, kuid andmete vähesus nende täpsema leviku kohta piirab edasise uurimise võimalusi. Antud lõputöö eesmärk on pakkuda süstemaatilist kõrge resolutsiooniga teavet HMM kohta Eesti Alam-Ordoviitsiumi kompleksides.

Töös käsitletavad lubjakivi, glaukoniitliivakivi, mudakivi ja fosforiidi proovid pärinevad PH012B puuraugust Aseris, Lääne-Virumaal. Stratigraafiliselt hõlmab uuritav vahemik Toila kihistust kuni Kallavere kihistuni. Selleks, et pakkuda HMM ja nende keemiliste ning mineraloogiliste muutujate kohta põhjalikku ülevaadet, analüüsiti multiinstrumentaalanalüüsiga (ICP-MS, XRF ja XRD) kokku 117 proovi.

Tulemuste kohaselt on lubjakivide HMM kogusisaldus keskmiselt 95±2 ppm, glaukoniitliivakivi puhul 142±2 ppm, mudakivi puhul 157±6 ppm ja fosforiitide puhul 1026±23 ppm. Kõigi komplekside keskmine kergete HMM (La, Ce, Pr, Nd) summa on 929,23 ppm, keskmiste HMM (Sm, Eu, Gd, Tb, Dy) summa on 161,07 ppm ja raskete HMM (Ho, Er, Tm, Yb, Lu) summa on 51,54 ppm. PAAS normaliseeritud HMM mustrid viitavad, et komplekside rikastustasemed on sarnased keskmise kildaga; fosforiidi puhul näitavad mõned HMM aga kuni kümnekordset rikastumist. Ühiseks jooneks on keskmiste HMM rikastumine. Eri kompleksides tuvastati Ce, Eu, Y anomaaliad. Lubjakivide puhul võib järeldada, et kaltsiidil ei olnud HMM akumulatsioonile suurt mõju ning mõõdetud HMM signaal on tõenäoliselt osaliselt pärit terrigeensest fraktsioonist. Glaukoniitliivakivis täheldatakse tugevat positiivset korrelatsiooni apatiidi ja HMM vahel, mis tõenäoliselt viitab HMM rikastumise seotusele apatiidiga. Arvestades, et mudakivis on HMM rikastumine statistiliselt seotud kvartsi ja apatiidi sisaldusega, on apatiit taas peamiseks HMM kandjaks. Fosforiidis leiduvatel HMM on teiste elementide ja apatiidi, dolomiidi ja MnO-ga kõige tugevam korrelatsioon. Nagu hiljutised uuringud on näidanud, siis keskmiste HMM rikastumine võrreldes teiste HMM-ga viitab etapiviisilisele HMM omastamisele ja fraktsioneerumisele merevees.

Selleks, et saada teavet valitsevate redokstingimuste ja HMM päritolu kohta, rakendati erinevaid elementaarse suhte määramismeetodeid. Ce anomaalia arvutuste põhjal sobitusid "anoksilisse" kategooriasse ainult fosforiidiproovid, kõik teised proovid langesid "suboksilisse" rühma. Lisaks andsid uuritud litoloogiate Y/Ho suhted valdavalt "terrigeense" sisendi signaali, välja arvatud fosforiidiproovid, millest enamik näitas rohkem mereveele sarnaseid jälgi. Ebakorrapärased Eu/Eu* signaalid lubjakivi ja mudakivi puhul võivad viidata Ba interferentsile Eu signaalidega ICP-MS analüüsil. Siiski võib see viidata ka võimalikele hüdrotermilistele või Mn-Fe ühendite mõjule diageneetilises keskkonnas. Töö käigus saadud andmed pakuvad hea baasi edasisteks põhjalikeks uuringuteks nii paleokeskkonna kui ka ressursside vaatenurgast.

List of Figures

Glossary of Abbreviations and Terms

HREE – heavy rare earth element

ICP-MS – inductively coupled plasma mass spectrometry

LOI – loss on ignition

LREE – light rare earth element

MREE – medium rare earth element

PAAS – Average Post-Archean Australian Shale

ppb – parts per billion

ppm – parts per million

ppt – parts per trillion

REE – rare earth element

XRD – X-ray diffraction

XRF – X-ray fluorescence

1. Introduction

The demand for energy and raw mineral resources rises every day due to urbanisation, improvements in well-being, higher living standards and production of advanced technologies. A global shift to green energy alternatives has triggered a need for rare earth elements (REEs). The demand for rare earth oxides from clean technologies is expected to reach 50 kt in 2030 (Dutta et al., 2016). The European Commission has created a list of critical raw materials based on their economic importance and supply risk. As of 2023, the list contains 34 critical materials (European Commission, 2023), including light rare earth elements (LREE) and heavy rare earth elements (HREE), but also phosphate rock and phosphorus, all of which can be potentially extracted from Estonian sedimentary phosphorite complexes. Further research is needed to understand the full potential of these local sedimentary deposits in terms of REE valorisation. Thus, for sustainable and environmentally safe extraction, the ability to accurately predict the amount and variability of REEs and carriers of those elements is crucial.

The thesis aims to provide a stratigraphically more extensive overview of the rare earth element distribution in Estonian Lower Ordovician complexes, along with currently under investigation REE-containing shelly phosphorites. Recent studies have explored the distribution of REEs in the latter, suggesting multistage uptake of REEs, which started during sediment accumulation and continued through early diagenesis (Graul, Kallaste, Pajusaar, et al., 2023; Lumiste et al., 2021). However, the scarcity of data on REE distribution within other associated lithologies (Kiipli et al., 2000; Voolma et al., 2013) limits the ability to further interpret the REE uptake pathways and local environmental controls on REE enrichment processes. Moreover, other sedimentary complexes, such as glauconite-rich rocks, have been explored as economically potential carriers of REEs in different localities (Kechiched et al., 2018). On a more general level, the development of specific enrichment patterns in case of what light, medium or heavy REEs are preferentially enriched in ancient marine sedimentary deposits, is still a debatable topic despite extensive research in this field (Bright, 2020; Lécuyer et al., 2004; Saltzman et al., 2011; Sholkovitz, 1990). Potential major control factors include REE distribution in seawater, fractionation of REEs related to different primary carriers such as Fe-Mn oxyhydroxides or organic matter, and admixture of REE-enriched terrigenous fraction to sediments (Abbott et al., 2019; Auer et al., 2017; Chen et al., 2023; Graul, Kallaste, Pajusaar, et al., 2023; Tadayon et al., 2024; Tostevin, 2021).

This is the first systematic high-resolution study on REE variability in Estonian Lower Paleozoic complexes using whole rock data of different lithologies. The samples for the study were collected from borehole PH012B in Aseri, Lääne-Virumaa. The rock complexes under investigation are limestone, glauconitic sandstone, mudstone and phosphorite. The stratigraphically studied interval spans from the Toila Formation (Volkhov Stage) to the Kallavere Formation (Pakerort Stage). The thesis excludes the black shale horizon (Türisalu Formation) due to the complex physicochemical nature and the challenges of interpreting results without additional research. Multi-instrumental (ICP-MS, XRF, and XRD) analyses were conducted using high-resolution sample sets from different rock complexes to provide a comprehensive overview of REEs and related chemical and mineralogical variables. The thesis consists of a literature review (rare earth elements, geological background of Estonian Lower Ordovician complexes, inductively coupled plasma mass

spectrometry analysis principles, X-ray fluorescence analysis principles, X-ray diffraction analysis principles), methodology description (data description, sampling and sample preparation), results (mineralogy of studied lithologies, major elements of the complexes and REE distribution) and discussion.

2. Literature Review

This chapter gives a synthesis of the main topics related to the thesis: an overview of rare earth elements, the geological background of the Lower Ordovician of Estonia, and used analytical methods: inductively coupled plasma mass spectrometry (ICP-MS) analysis, X-ray fluorescence (XRF) analysis, X-ray diffraction (XRD) analysis.

2.1. Rare Earth Elements

The International Union of Pure and Applied Chemistry (IUPAC) defines rare earth elements as a set of 17 metallic elements that share chemical similarities, comprising 15 lanthanides (from La to Lu) alongside yttrium (Y) and scandium (Sc), which have similar chemical and physical properties (Zhou et al., 2017). REEs are divided into light rare earth elements (LREE – La, Ce, Pr, Nd, Pm), sometimes medium rare earth elements (MREE – Sm, Eu, Gd, Tb, Dy) and heavy rare earth elements (HREE – Ho, Er, Tm, Yb, Lu, Y), not including Sc, which falls outside this categorisation (Jaireth et al., 2014).

Rare earth elements were first discovered in 1788 and are, in fact, not rare and have a broad geological distribution (Zhou et al., 2017). All lanthanides occur in nature, although Pm, which is radioactive, is not found in significant quantities (Elkina & Kurushkin, 2020). Ce is the most abundant, followed by La; Tm and Lu are the least abundant. REEs are typically enriched together in the Earth's crust due to their common trivalent charge (REE^{3+}) and similar ionic radii. Notable exceptions include Ce, which can also occur widely in nature in a Ce^{4+} valence state, and Eu, which can exist as Eu^{2+} (Van Gosen et al., 2017). The average concentrations of REEs in the Earth's crust range from 150 to 220 parts per million (ppm), which surpasses the concentrations of many other metals mined for industrial purposes (Dutta et al., 2016).

REEs can be found in a wide range of mineral types, including halides, oxides, carbonates, phosphates and silicates. Over 200 minerals are known to contain REE, although a small number has the potential to become commercially significant. Mineral deposits of REE can occur in a broad range of igneous, sedimentary and metamorphic rocks (British Geological Survey, 2011). China, which has dominated global REE production for decades, has accounted for over 90% of worldwide production and supply on average over the past decade (Van Gosen et al., 2017).

Rare earth elements are used in a wide range of technologies, for instance optical, magnetic, and catalytic applications (Figure 1). They also occupy a vital role in the green transition, particularly in the production of wind turbines (Zhou et al., 2017). Additionally, media and communication devices such as cell phones, televisions, and computers, use rare earth elements in various components, including magnets for speakers and hard drives, as well as phosphors for optical displays (British Geological Survey, 2011).
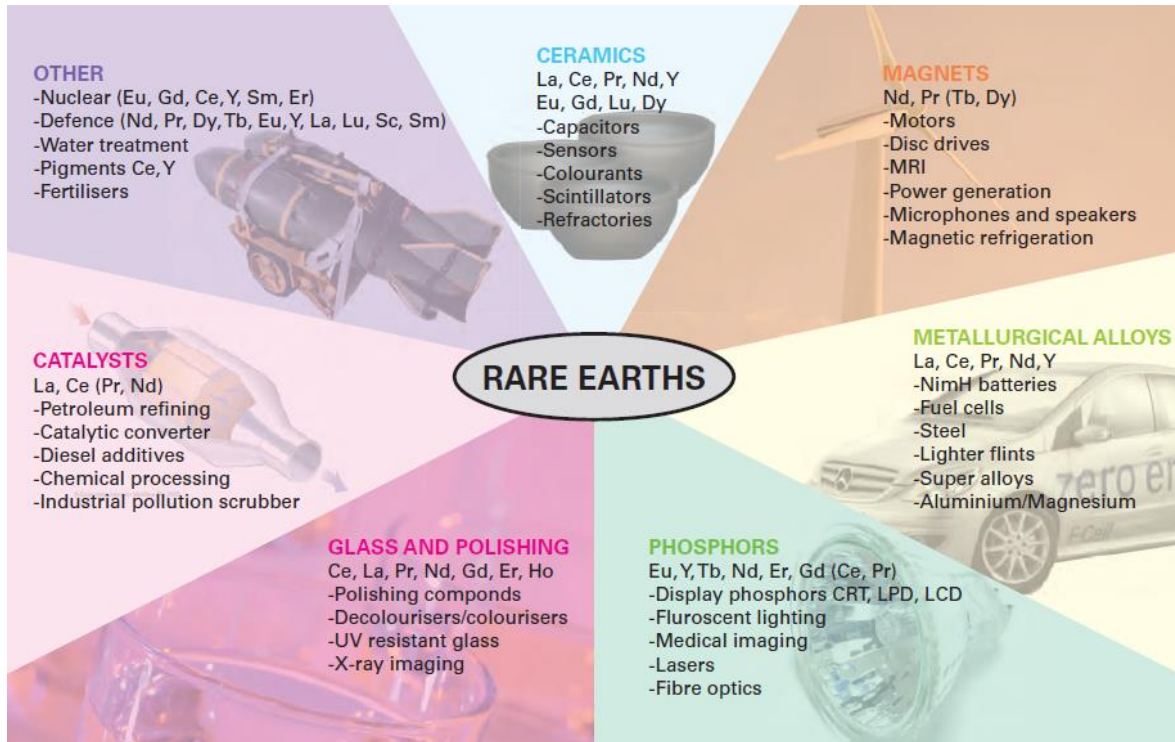
Figure 1. Rare Earth Elements applications (British Geological Survey, 2011).

Moreover, REEs can be used as proxies for paleoenvironmental studies to reconstruct ancient environmental conditions, to understand the geological history recorded in different complexes, and to trace geochemical processes. For example, the redox conditions in seawater (Shields & Stille, 2001), depositional environments and diagenetic processes (Bau & Dulski, 1996), and oceanic and atmospheric oxygen levels (German & Elderfield, 1990) can be investigated based on Ce anomaly calculations (Tostevin et al., 2016).

2.2. Geological Background of Estonian Lower Ordovician Complexes

Estonia is located on the East European Craton, which forms a part of the Baltica paleocontinent. The crust in this region consolidated during the Svecofennian Orogeny in the Paleoproterozoic. Crystalline basement rocks are overlain by sedimentary layers from the Late Proterozoic (Ediacaran) to the Lower Paleozoic (Cambrian, Ordovician, Silurian and Devonian). The thickness of these sedimentary deposits varies from 100 meters in the north to 800 meters in the south of Estonia, because the surface of the crystalline basement dips to the south (Raukas & Teedumäe, 1997; Soesoo, 2022). The Ordovician period, from 488 to 443 million years ago, is characterised by the dominance of marine environments (Nestor et al., 2007). Ordovician rocks are extensively distributed throughout the Baltoscandian region. In the East European Platform, these strata extend from the Baltic Sea islands in the west to the vicinity of Moscow in the east, and from the Gulf of Finland in the north to Belarus and Poland in the south (Figure 2). The overall thickness of the Ordovician strata in Estonia ranges from 70 to 180 meters, with the greatest thickness observed in central and eastern Estonia, and the thinnest in the outcrop area of Baltic Klint and southwestern mainland of the country (Meidla et al., 2014).
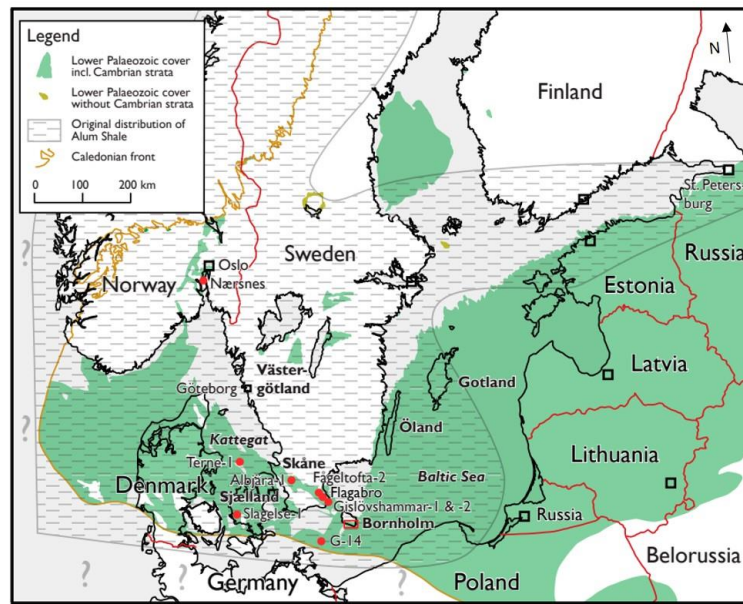
Figure 2. Distribution of Lower Ordovician complexes in Baltoscandia. Modified after Nielsen et al. (2018).

The Ordovician succession of Estonia commences with the upper segment of the Kallavere formation (Figure 3), characterised by brownish-grey, medium-grained, weakly cemented **quartz sandstone** (phosphorites) typically 4–10 meters thick, but locally reaching up to 20 meters. This unit is overlain by **dark brown bituminous argillites** (black shales) of the Türisalu Formation, up to 6 meters thick, and **light grey clays** (mudstones) of the Varangu Formation, up to 4 meters thick. Above these layers, the Leetse Formation stands out as a marker unit of dark green, **glauconite-rich quartz sandstones**, which reach up to 4.5 meters in northern Estonia but less than 1 meter in central Estonia. The contact between this sandstone and the overlying carbonate strata of the Toila Formation is sharp. The boundary of Lower and Middle Ordovician is also located in the lower part of the Toila Formation, which is composed of **pure and argillaceous limestones**, locally dolomitised and containing glauconite. The uppermost Lower Ordovician is primarily composed of diverse **limestones and marls**, occasionally dolomitic, interspersed with infrequent occurrences of **dolomites and argillites** (Meidla et al., 2023; Raukas & Teedumäe, 1997).

The alteration in sedimentation type and biofacies characteristics is attributed to a progressive climatic shift caused by the northward movement of the Baltica paleocontinent from the temperate climatic zone to the (sub-) tropical region (Meidla et al., 2014). Estonia is renowned for studying major evolutionary and paleoenvironmental changes from the Cambrian to Upper Devonian periods (Harper et al., 2023; Saltzman et al., 2011; Trotter et al., 2008).
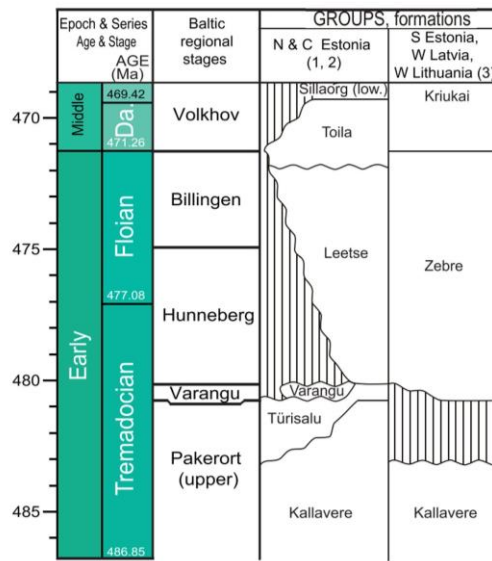
Figure 3. Stratigraphy of Lower Ordovician in Estonia. Modified after Meidla et al. (2023).

The Furongian (Cambrian) to Lower Ordovician shallow marine complexes in Estonia, which formed in shallow water inner shelf of the epicontinental Baltic Paleobasin, contain potential sedimentary mineral resources such as shelly phosphorites and metalliferous black shales (Ndiaye, Liiv, et al., 2023). Due to the scarcity of organisms with calcareous skeletons, sedimentation during the Early Ordovician was slow and discontinuous (Nestor et al., 2007). The shift from terrigenous to carbonate rocks during the Billingen Stage is indicated by the emergence of calcareous interbeds within the siltstones. The lower part of carbonate succession was characterised by numerous hiatuses and episodes of glauconite deposition and ferruginous ooids accumulation in nearshore regions (Meidla et al., 2023). The Ordovician limestone sequence in Estonia commences with cold-water carbonates laid down in a shallow marine basin with limited sediment supply, but increasing sedimentation rates (Meidla et al., 2014).

2.3. Inductively Coupled Plasma Mass Spectrometry (ICP-MS) Analysis Principles

Inductively Coupled Plasma Mass Spectrometry (ICP-MS) is an analytical technique used for the detection and quantification of trace elements and isotopes (Makonnen & Beauchemin, 2020). Due to its unique properties, including high sensitivity, multi-element capabilities, a wide linear range, and the ability to obtain isotopic information, numerous applications across various fields such as geochemistry, environmental studies, clinical and biological materials, can be used (Meermann & Nischwitz, 2018).

ICP-MS typically has a scanning quadrupole mass filter and a detector, an ICP-MS instrument which operates with the ICP at atmospheric pressure and the MS and detector in a vacuum chamber. The fundamental principle employed in ICP-MS is the use of a high-temperature Ar plasma discharge to generate positively charged ions by exciting the outer electron of a ground-state atom to generate photons of light with specific wavelengths, subsequently quantified using a mass spectrometer (Agilent Technologies, 2024). The sample, which is usually in liquid form, is introduced into a spray

chamber and a nebuliser. It exits as an aerosol and is subsequently directed, via a sample injector, into the base of the plasma. Progressing through various heating zones within the plasma torch, the sample undergoes drying, vaporisation, atomisation, and ionisation. Over this process, the sample transitions from a liquid aerosol to solid particles, and eventually into a gas state. Upon reaching the analytical zone of the plasma, at temperatures around 6000–7000 K, it exists as excited atoms and ions, representing the elemental composition of the sample (Thomas, 2001).

ICP-MS offers a comprehensive capability to measure virtually every naturally occurring element and numerous non-natural 'radiogenic' isotopes. However, there are certain limitations to note. For example, elements such as H and He fall below the mass range of the mass spectrometer and therefore cannot be measured. Additionally, Ar, N, and O, which are present at high levels from the plasma and air, cannot be accurately measured using ICP-MS. Furthermore, F and Ne cannot be ionised within an Ar plasma, thus precluding their measurement with this technique. Understanding these limitations is crucial for accurate and reliable analysis when utilising this instrumentation. ICP-MS is highly demanded due to its remarkable sensitivity, offering detection limits well below 0.1 ppt for most measurable elements. This exceptional sensitivity makes ICP-MS an invaluable tool for trace element analysis in various fields (Agilent Technologies, 2024; Thomas, 2001). To achieve accurate and precise isotope ratios, meticulous attention is required during sample preparation, instrument optimization, and mass bias correction (Yang, 2009).

2.4. X-Ray Fluorescence (XRF) Analysis Principles

XRF (X-ray fluorescence) is a non-destructive analytical technique used to ascertain the elemental composition of materials (Oyedotun, 2018). Various sample types, such as solids, liquids, and loose powders, can be analysed. By measuring the fluorescent (secondary) X-rays emitted from a sample when stimulated by a primary X-ray source, XRF analysers determine the sample's chemistry. Each element in the sample generates a distinct set of characteristic fluorescent X-rays, making XRF spectroscopy an exceptional tool for qualitative and quantitative analysis of material composition (Bruker, 2024; ThermoFisher, 2020).

A typical XRF spectrometer consists of an X-ray source, a sample chamber, a possible crystal analyser, a detector and a signal processing instrument. Various detector types, including gas flow proportional and scintillation detectors, are utilised to measure the intensity of the emitted beam (Bruker, 2024; Schramm, 2016). XRF instrumentation is categorized into two main types: wavelength-dispersive X-ray fluorescence (WDXRF) and energy-dispersive X-ray fluorescence (EDXRF). The primary difference between these two systems lies in how they distinguish the energies of X-ray photons emitted from the sample. WDXRF uses a crystal to achieve high resolution, while EDXRF employs a semiconductor detector (Marguí et al., 2022).

A sample is irradiated with high-energy X-rays from a controlled X-ray tube. When an atom in the sample absorbs an X-ray with energy greater than its K or L shell binding energy, an electron from one of its inner orbital shells is ejected. The atom subsequently stabilises by filling the vacant inner orbital shell with an electron from a higher energy orbital shell. As the electron transitions to the lower energy state, it emits a fluorescent X-ray (Figure 4). As X-ray energy prompts electron

transitions between shell levels, varying intensities of XRF peaks are generated and observed in the spectrum. The peak energy identifies the element, while the peak height or intensity typically reflects its concentration (Bruker, 2024; ThermoFisher, 2020).
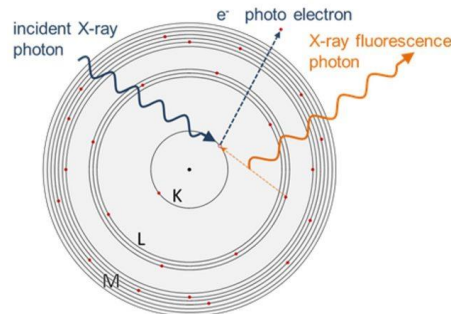
Figure 4. XRF process sketch (Bruker, 2024).

The result of XRF analysis is strongly dependent on sample preparation. Techniques include XRF pressed pellets and XRF fusion technique (Potts, 1987). The pellet technique is rapid and simple; however, fusion gives higher precision with an ideally homogeneous sample but includes dilution and therefore is rational to analyse only the major elements. XRF analysis cannot make a difference between variations in the isotopes of an element (Schramm, 2016).

2.5. X-Ray Diffraction (XRD) Analysis Principles

X-ray diffraction (XRD) serves as a non-destructive analytical method enabling the exploration of diverse crystalline material phases. While elemental analysis facilitates identifying and quantifying constituent chemical elements, XRD offers a comprehensive understanding of element arrangement within a material, focusing on its crystal lattice. XRD allows the determination of mineralogical composition based on obtained diffractograms (Malvern Panalytical Ltd, 2024; Speakman, 2011).

The periodic lattice arrangement of atoms in a crystal enables the diffraction of light. The scattering of X-rays from atoms produces a diffraction pattern, which gives information about the atomic arrangement within the crystal. The location of the diffraction peaks is dictated by the spacing between parallel planes of atoms (Speakman, 2011). The Bragg's law in Equation 1 computes the angle at which constructive interference occurs, resulting in the formation of a diffraction peak from X-rays scattered by the parallel planes of atoms:

$$n\lambda = 2d \sin\theta, \tag{1}$$

where n is an integer (1, 2, 3,…), d marks the interplanar spacing creating the diffraction, and θ is the X-ray incident angle (Khan et al., 2020). The atoms within the crystal, owing to their regular arrangement, generate a pattern of constructive interference from the waves within the scattered X-ray beam (Speakman, 2011).

The main parts of an X-ray instrument are an X-ray source, a sample holder and an XRD detector. Within an X-ray diffractometer, distinct crystalline phases yield unique diffraction patterns. The X-

rays produced by the source illuminate the sample. A finely ground and homogenised sample is required to determine of the bulk composition. It is then diffracted by the sample phase and enters the detector. By moving the tube or sample and detector to change the diffraction angle (2θ, the angle between the incident and diffracted beams), the intensity is measured, and diffraction data are recorded (Figure 5). Identification of these phases entails comparing the X-ray diffraction patterns of unknown samples with those stored in reference databases. The Rietveld method is a semi-quantitative technique that adjusts selected parameters to minimise the disparity between an experimental profile and a model derived from the theoretical crystal structure and instrumental parameters (Malvern Panalytical Ltd, 2024; Speakman, 2011).
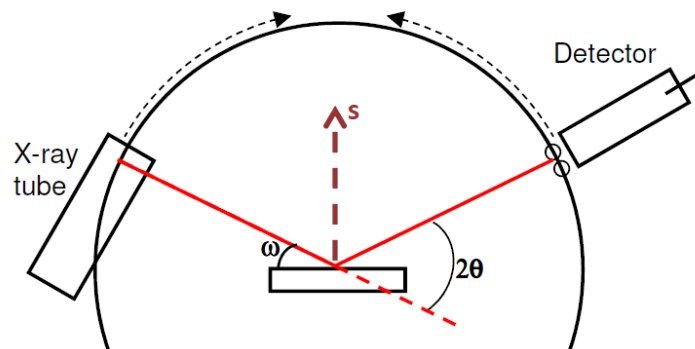
Figure 5. Diffractometer scheme (Speakman, 2011).

3. Methodology

To provide an overview of the distribution of rare earth elements in Estonian Lower Ordovician complexes, ICP-MS, XRF, and XRD analyses were conducted on selected samples from the Aseri PH012B borehole. The following subchapters describe the data selection process, sample preparation, and the details of executing the analysis. All the sampling and analytical studies were carried out at the Department of Geology, Tallinn University of Technology.

3.1. Data of Aseri PH012B Borehole

To investigate the distribution of rare earth elements in Estonian Lower Ordovician complexes, the borehole PH012B was chosen (59.426053, 26.755267). It is located 7 km southwest of Aseri, Estonia (Figure 6). The borehole penetrates rock complexes from the Väo Formation (Uhaku Stage, Middle Ordovician) to the Tiskre Formation (Series 2, Cambrian) including limestone, glauconitic sandstone, mudstone, black shales, phosphorite, and sandstone (Meidla, 2020; Meidla et al., 2014). The drill core was drilled by the Geological Survey of Estonia in 2020. The diameter of the drill core is 85 mm, and the total length is 27.2 m. The core recovery is 100% for most of the core (eMaapõu, 2024).

This borehole was chosen as several high-resolution geochemical investigations have recently been conducted using considered section (Graul, Kallaste, Moilanen, et al., 2023; Ndiaye, Liiv, et al., 2023; Ndiaye, Pajusaar, et al., 2023). Furthermore, it is located within the Rakvere Phosphorite Region where active exploration of phosphatic sandstones and related rare earth elements resources is ongoing. Nevertheless, besides phosphorites, little is known about rare earth distribution in other Lower-Palaeozoic sedimentary rocks in the study area. The lithology of the borehole is summarised in the Figure 7.

Figure 6. Borehole PH012B location. Aseri, Lääne-Virumaa (Estonian Land Board, 2024).
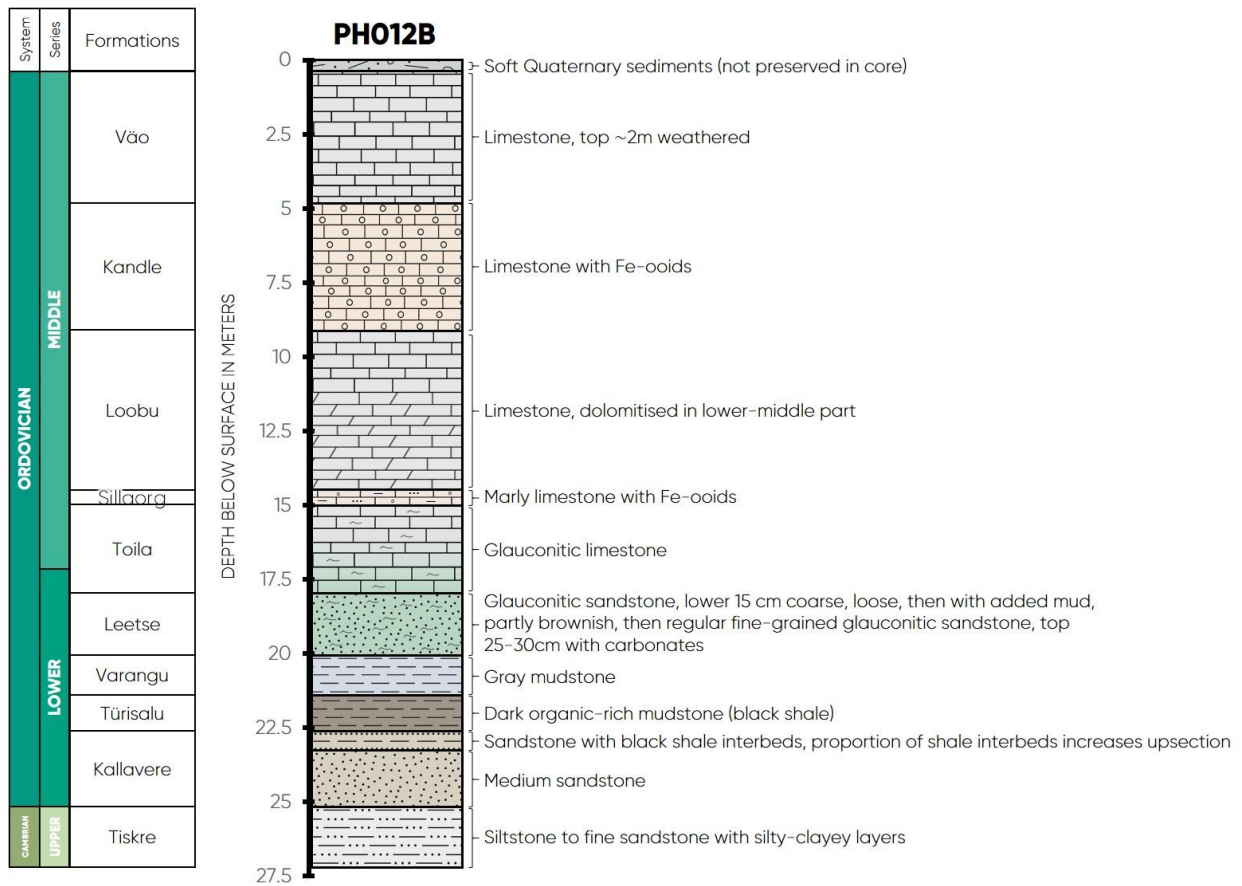
Figure 7. Lithostratigraphic column of drill core PH012B. The lithological description is based on eMaapõu (2024).

3.2. Rock Complexes Selection and Sampling Resolution

Different rock complexes were selected to investigate the rare earth element distributions: limestone, glauconitic sandstone, mudstone and phosphorite (drill core boxes 5, 6, 7, 8). Black shales are omitted from this thesis because of their physicochemical complexity and difficulty in interpreting the results without further research. Samples were prepared for instrumental studies, and a systematic dataset was compiled, representing 203 samples between depths 14.49-21.34 m (Figure 8). Unpublished data of phosphorite samples (depths 23.65-25.17 m) and some mudstone samples (depths 21.34-21.55 m) published by Ndiaye, Pajusaar, et al. (2023), had been included to the analysed data set.
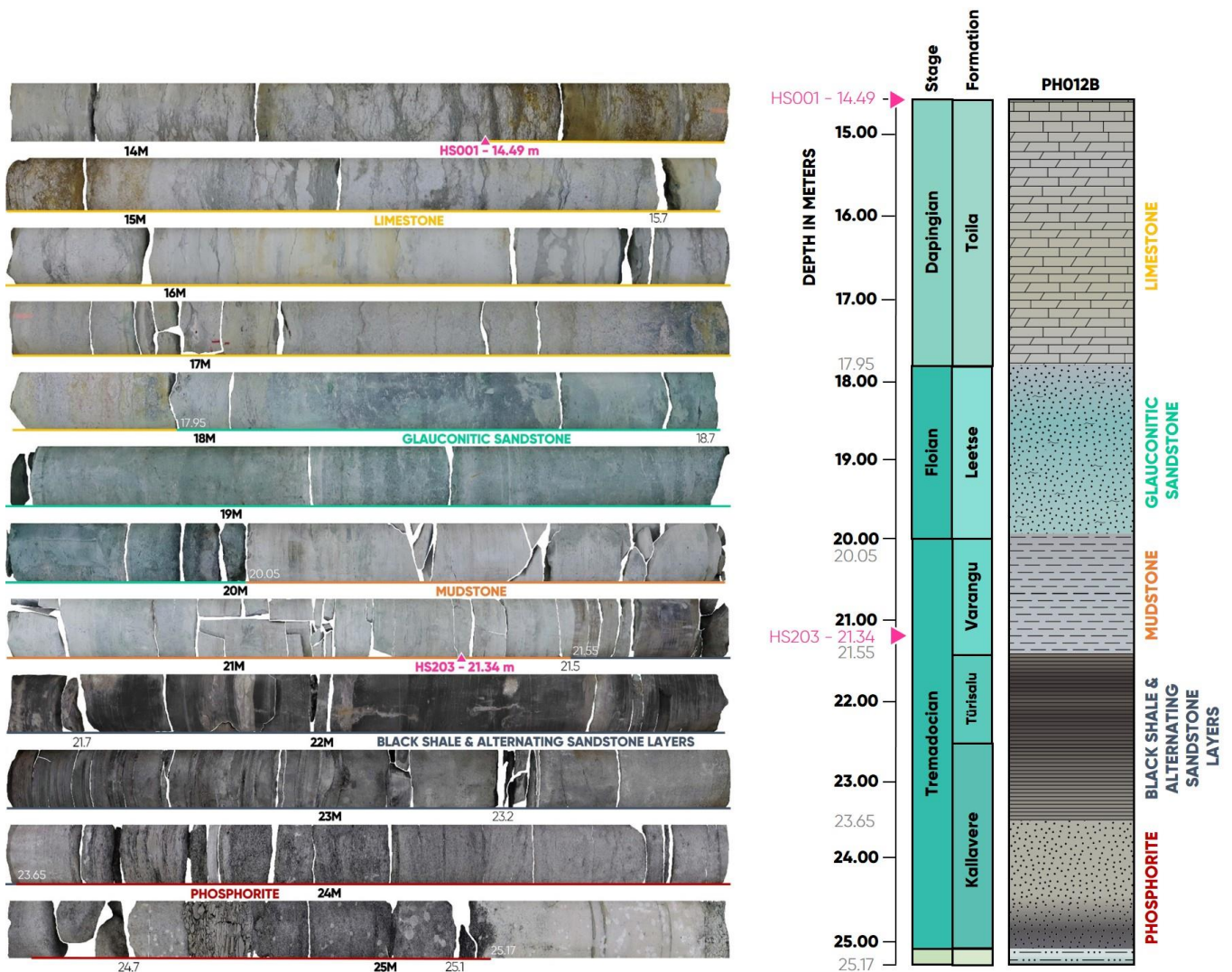
Figure 8. Drill core PH012B with selected sampling intervals, rock complexes and a lithological profile. The depth between HS001 – 14.49 m and HS203 – 21.34 m marks the region in which the samples were collected and prepared by the author.

3.2.1. Descriptions of Selected Rock Complexes

The overall observations of selected rock complexes of limestone, glauconitic sandstone, mudstone and phosphorite are described more in detail in the following paragraphs.

a) Limestone

The varicoloured limestones of the Toila Formation present different lithological varieties ranging from greenish grey to brown shades (Figure 9). The upper part of the studied limestone drill core cross-section contains Fe-ooids and the lower part, green glauconitic grains. The formation also presents argillaceous laminae, discontinuity surfaces, nodular features, and small caverns.
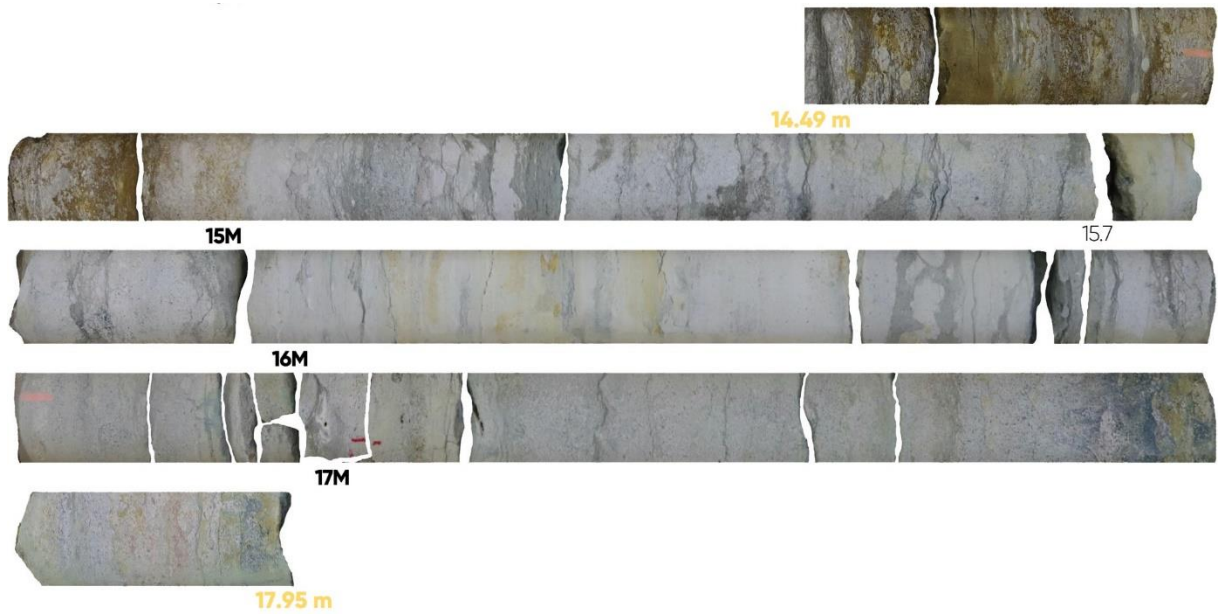
Figure 9. Selected limestone section from the studied drill core (depths 14.49-17.95 m).

b) Glauconitic sandstone

The glauconitic sandstone of the Leetse Formation presents a lithologically heterogeneous section with varying grain sizes from sandstone to mudstone and different shades of greenish-greyish colour due to the distribution of glauconite distribution (Figure 10).

Figure 10. The glauconitic sandstone section from the studied drill core (depths of 17.95-20.05 m).

c) Mudstone

The mudstone from the Varangu Formation is mostly grey and presents a homogenous aspect, with generally well-preserved horizontal (micro-) lamination (Figure 11). The lower part shows darker shades, in transition with the black shales.
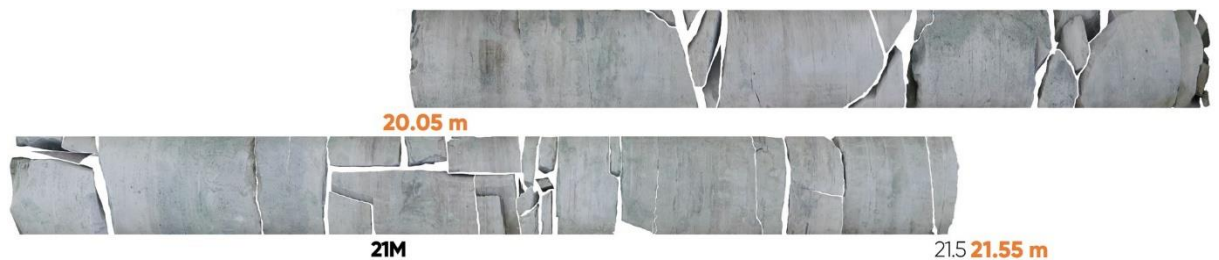
Figure 11. The mudstone section from the studied studied drill core (depths of 20.05-21.55 m).

d) Phosphorite

The phosphorite section (the lower part of the Kallavere Formation) comprises a basal cemented coquina layer, followed by horizontal to cross-laminated sandstones with phosphatic detritus of brachiopods. The upper horizons comprise sandstone with black shale interbeds (Figure 12).
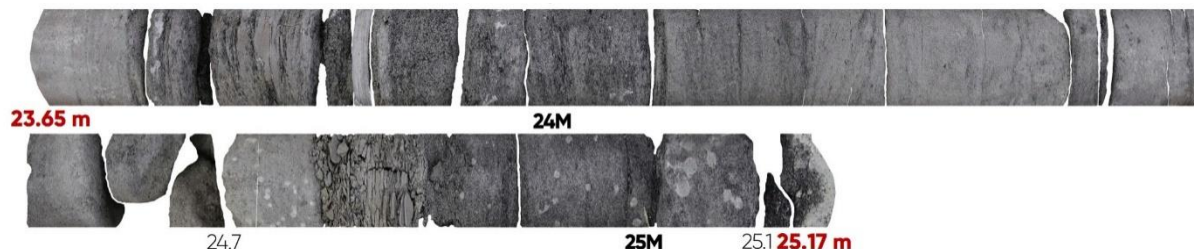
Figure 12. Phosphorite section from the studied drill core (depths 23.65-25.17 m).

3.2.2. Sampling Resolution

High sampling resolution (small sizes of the core samples) was selected to explore rock complexes and capture potential primary or diagenetic variation in rare earth element distributions. The sampling interval for limestone and glauconitic sandstone (depths 14.49 m to 20.05 m) was set to 5 cm and for mudstone samples (depths 20.05 m to 21.34 m) to 1 cm. The phosphorite samples have a resolution of 5 cm. Initially, continuous sampling of the core section was carried out for targeted horizons. However, as the preparation and analysis processes are time-consuming, the number of limestone and mudstone samples was reduced by picking selected materials in regular intervals. Thus the number of samples analysed is lower than the number of samples prepared initially (Table 1).

Table 1. Rock complexes and sampling resolution.

Complex name	Depths	Number of samples prepared	Prepared samples resolution	Number of samples analysed	Analysis resolution	Remarks
Limestone	14.49-17.95 m	70	5 cm	24	15 cm	Samples prepared and analysed by the author
Glauconitic sandstone	17.95-20.05 m	44	5 cm	44	5 cm	
Mudstone	20.05-21.34 m	89	1 cm	19	5 cm	
	21.34-21.55 m	-	-	4	5 cm	Samples prepared beforehand
Phosphorite	23.65-25.17 m	-	-	26	5 cm	
Samples in total	-	203	-	117	-	87 samples were prepared and analysed by the author in total

3.3. Sampling and Sample Preparation

The first sampling step was to clean the drill core of residue material from previous cutting and transportation, which was started in February 2024. The selected drill core segments were then cut into regular pieces with a saw and crushed and milled afterwards (Figure 13). 203 samples were collected in total: 70 limestone samples (HS001-HS070), 44 glauconitic sandstone samples (HS071-HS114), and 89 mudstone samples (HS115-HS203).
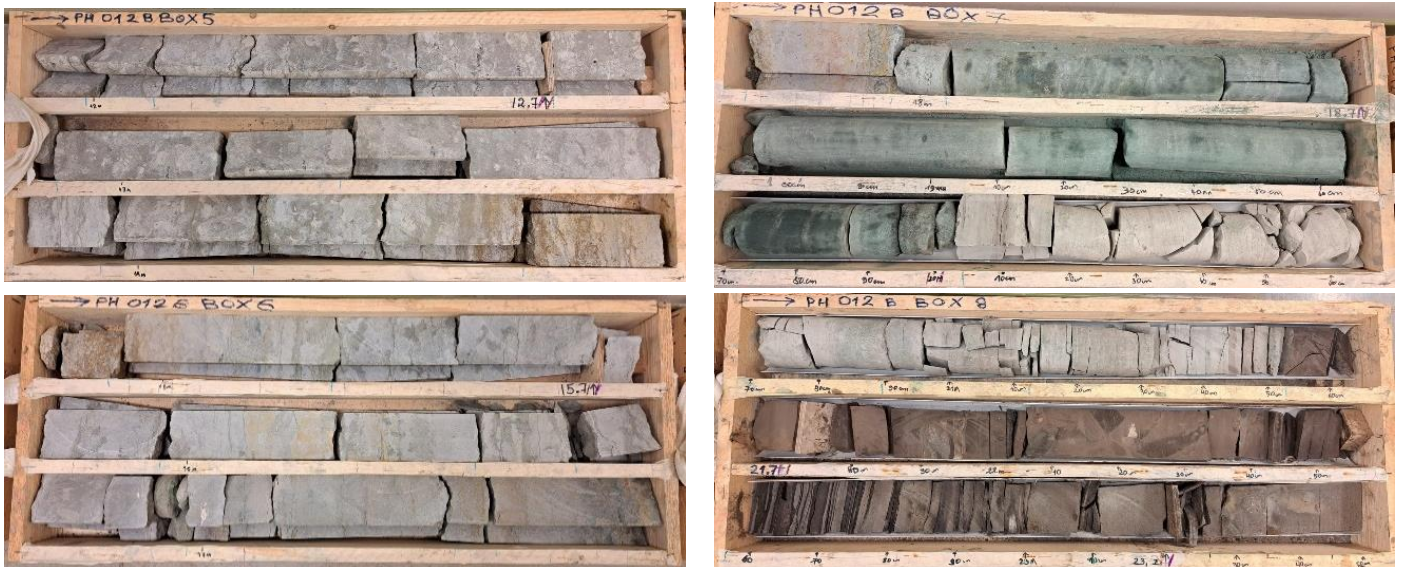
Figure 13. Aseri PH012B drill core boxes 5, 6, 7, and 8 before sampling.

3.3.1. Cutting

For limestone sampling, 1/8 of the drill core segment was processed; for glauconitic sandstone and mudstone, 1/4th of the drill core was cut, respectively. Small pieces of rocks that broke apart from the drill core segments during cutting made the sampling procedure highly challenging, especially for the mudstone part. Drill core segments were further cut to obtain intervals according to the sampling schema explained beforehand. To preserve the 1 cm samples in the correct layout and order, pieces were marked with an arrow, and paper clips were used to separate the cut samples (Figure 14).

Figure 14. Mudstone samples are divided by papers to keep the layout and order.

3.3.2. Crushing

The first comminution steps for limestone and glauconitic sandstone were conducted with a Retsch jaw crusher. Crushing was done to reduce samples to a 10-20 mm fraction, and after, to 2-2.5 mm. Mudstones were crushed with a hammer between paper towel sheets.

3.3.3. Milling

Materials were ground using a tungsten-carbide grinding set and the Rocklabs Benchtop Ring Mill. The milling time was set at 3 minutes, and each sample grain size was checked to ensure a sufficiently fine grain sine. The grinding set had to be cleaned between each sample, and after every 10 samples or the change of rock complexes, milling with abrasive quartz powder was used to remove impurities. Some glauconitic sandstone samples turned out to have larger grains during the analysis preparation and had to be milled again before continuing sample preparations for analysis.

3.4. ICP-MS Analysis Methodology

Rare earth quantification in with ICP-MS required complete digestion of samples and several dilution steps to bring down the total dissolved solids concentration in the solution. Procedures and parameters used for the ICP-MS analysis are summarised in the following subsections.

3.4.1. Sample Preparation for ICP-MS Analysis

The sample preparation for ICP-MS analysis involved measuring the loss on ignition (LOI) and preparing sample solutions with borate fusion and dilution.

a) Measuring the loss on ignition

The sample preparation for ICP-MS analysis began with oxidising the materials at 950°C to obtain the LOI and to ensure the removal of moisture and volatiles (organic content, carbon dioxide and hydrated compounds). The LOI process:

- Ceramic crucibles were weighed with Mettler Toledo weight.
- 2.5 grams of finely crushed sample powder was weighed into crucibles.
- Crucibles with samples inside were put for 30 minutes to an hour into the drying cabinet to remove any excess moisture from the samples.
- After taking the samples out, samples were weighed again.
- Samples were then put into a muffle furnace. Settings used - 4 hours of heating the samples at 950°C.
- The LOI was measured by weighing the crucibles with samples inside. Oxidised samples were removed from the crucibles, homogenised in a mortar, and then stored.

b) Preparing the ICP-MS first dilution and conducting the fusion

50 ml tubes, Teflon beaker cups, magnets, 10% and 1% HNO_3 solution, ceramic crucibles, ultra-pure lithium borate flux, platinum crucibles, were used for those procedures. The following steps were applied for aliquot preparation:

- 0.1 g of oxidised sample powder and 1 g of borate flux were weighed into ceramic crucibles, mixed with a vibrating shaker, and poured into platinum crucibles.
- The platinum crucibles were then set, the Teflon beaker cups were filled with 45 ml of 10% HNO_3 solution and a magnet was put in each of the cups. Fusion was conducted by using Claisse M4 fusion instrument.
- After fusion magnets stirred the liquid inside Teflon beaker cups. Any drops stuck on the crucibles were removed and transferred into the beaker cups to ensure full recovery.
- When the sample was completely dissolved, homogenised content was poured into a 50 ml tube. 1% HNO_3 solution was finally added to fill up to 50 ml.
- Rigorous cleaning procedures were applied for the used equipment before preparing the next sample batch.

c) Preparing the ICP-MS second dilution

For the second dilution step 10 ml tubes, 50 ppb bismuth and 50 ppb indium internal standard solutions, 1% HNO3 solution, first dilution tubes, a pipette and safety equipment were used. The process is described below:

- 1 ml of Bi and In standard solutions were added to the 10 ml tube.
- 0.5 ml of the solution from the first dilution tube added to the same 10 ml tube.
- 7.5 ml of 1% HNO_3 solution was then poured. The total solid content (TDS) was calculated. Total sample dilution rates were in the range of 8000 to 9000.
- Pipette tips were replaced after each use to ensure maximum precision.

3.4.2. Conducting the ICP-MS Analysis and Data Obtained

ICP-MS analysis was performed using a Thermo Scientific iCAPQ instrument for the measurement of quantitative elemental concentration of 50 trace and major elements (or their dominant naturally occurring isotopes) such as: Na, Mg, Al, P, K, Ca, Ti, V, Cr, Mn, Fe, Co, Ni, Cu, Ga, Ge, As Zn, Se, Rb, Zr, Nb, Mo, Ag, Cd, Sn, Sb, Te, Cs, Ba, La, Ce, Pr, Nd, Sm, Eu, Gd, Dy, Ho, Er, Tm, Yb, Lu, Hf, Ta, W, Tl, Pb, Th, U. Element calibration solutions for ICP-MS were prepared from multi-element calibration solutions. Each calibration solution set was prepared in four concentrations: 1, 10, 100 and 1000 ppb. Calibration curves were linear and forced through blank. The coefficient of determination of the calibration curves was typically in the range of 0.999 to 0.9999.

Quantitative measurement of element concentration was measured at two different modes – a kinetic energy discrimination (KED) mode (also referred to as Collision Cell Technology) for the elements with an atomic weight from 45 to 85; and a standard mode for other elements. In KED mode, a gas mixture of 8% hydrogen in helium is fed into the mass spectrometer to reduce the interference. Argon was used as the plasma gas. Measurement results were automatically corrected for drift and matrix effects (matrix loading) using internal standard recovery. The working principle of ICP-MS analysis is described in paragraph 2.3 Inductively Coupled Plasma Mass Spectrometry (ICP-MS) Analysis Principles.

3.5. XRF Analysis Methodology

The XRF measurements conducted for the current study consisted of analysis of XRF fused discs and powdered pressed pellets. The settings used for sample preparation, analysis and different data treatment parameters are listed in the following paragraphs.

3.5.1. Sample Preparation for XRF Disc Analysis

The sample preparation for XRF disc analysis involves measuring the loss on ignition (LOI), sample preparation for fusion, and conducting the fusion. The process of measuring the loss on ignition has been described earlier in chapter 3.4.1 and is conducted identically.

a) Preparation of fused discs

The preparation for XRF fusion started with preparing ceramic crucibles, pure borate flux, platinum crucibles, and platinum crucible moulds.

- Ceramic crucibles were weighed with Mettler Toledo weight.
- 10 grams of pure borate flux and 1 g of oxidised (LOI) sample powder were also weighed, added into the ceramic crucibles, and mixed thoroughly.
- The prepared mix was added into platinum crucibles and fusion was conducted using fusion instrument Claisse M4. The melt was cast into mould and afterwards, XRF discs were labelled.

3.5.2. Sample Preparation for XRF Pellet Analysis

The sample preparation for XRF pressed pellet analysis started with preparing a 5% Mowiol glue (CH_2CHOH) solution, hydraulic pellet press equipment, and miscellaneous lab items such as a mortar with pestle and a syringe. The process is as described below:

- 8-8.5 grams of finely crushed sample powder was added into the mortar and homogenised with a pestle.
- 4-5 drops of 5% Mowiol glue was added to the sample using a syringe. The glue drops were covered with sample powder and mixed with the pestle 2-3 times to ensure homogenisation. The mix was transferred into the press mould.
- Prepared mould with sample was put under the press and 5 tonnes of maximum pressure was applied to compress the powder. The pellet was then taken out of the press mould, labelled, and dried for 10-15 minutes.

3.5.3. Conducting the XRF Analysis

To conduct the XRF analysis and analyse XRF discs and pellets, a Bruker S4 Pioneer wave dispersive XRF spectrometer was used. Already existing in-house calibrations based on internationally acknowledged comparative tests were employed. The apparatus operates at 3 kW with a rhodium X-ray tube. One measurement takes approximately 15 minutes for XRF discs, and 30 minutes for XRF pellets. The working principle of XRF analysis is described in paragraph 2.4 X-Ray Fluorescence (XRF) Analysis Principles. Spectra PLUS and a tool called EVAL2 were used to investigate the results. The XRF analysis of fused glass discs provided mass percentages of major elements in oxide format:

SiO_2, TiO_2, Al_2O_3, Fe_2O_3, MnO, MgO, CaO, Na_2O, K_2O, P_2O_5, SO_3). Measurements of pressed pellets also provided concentrations of major compounds (the list above plus S and Cl), but were used to provide volatile, such as F and CO_2, and 23 minor components data (As, Ba, Br, Ce, Co, Cr, Cu, Ga, La, Mo, Nb, Ni, Pb, Rb, Se, Sr, Th, U, V, W, Y, Zn, Zr). The data of the XRF disc analysis is used to correct the results of the XRF pellet analysis. The results of XRF discs are calculated for the initial sample (including the mass percentage of LOI).

3.6. XRD Analysis Methodology

The XRD analysis methodology consists of sample preparation, analysis and data treatment based on Rietveld refinement to interpret the semi-quantitative mineral composition. The settings used for analysis and different data treatment parameters used are listed in the following paragraphs.

3.6.1. Sample Preparation for XRD Analysis

The sample preparation for XRD analysis starts with preparing a mortar and a pestle, ethanol and an XRD specimen holder. The material was prepared as follows:

- Approximately 0.1 grams of finely crushed sample powder was put into the mortar, 0.1 g of alcohol was added, and the mix was homogenised with a pestle.
- The sample was smeared evenly across the surface of the sample holder, put in the drying cabinet, and analysed.

3.6.2. Conducting the XRD Analysis

XRD analyses were performed with a Bruker D8 ADVANCE Bragg-Brentano X-ray diffractometer at 35 kV, 40 mA and the wavelength of 1.79 Å was used. The machine is equipped with a Co Kα1 source and LYNXEYE detector. The diffraction data was collected between 5° and 56° as 2θ. One measurement took approximately 18 minutes. The working principle of XRD analysis is described in paragraph 2.5 X-Ray Diffraction (XRD) Analysis Principles. The Bruker DIFFRAC SUITE software package EVA and a reference database (Crystallography Open Database) were used to determine the minerals that are occurring. The main software used for XRD patterns analysis is DIFFRAC.TOPAS, utilising Rietveld's method for profile fitting. With XRD analysis semi-quantitative mineral contents of dolomite, Ca-dolomite, orthoclase, quartz, pyrite, calcite, chlorite, muscovite, anatase, apatite-CaF, sanidine, goethite, zircon and glauconite were obtained for different rock complexes.

4. Results

The results summarise multi-instrumental (ICP-MS, XRF and XRD) data obtained from **limestone**, **glauconitic sandstone**, and **mudstone** samples from the Aseri PH012B core, collected and prepared for the thesis by the author, as well as unpublished results of some mudstone samples and the whole set of **phosphorite** samples which have been recently analysed using similar study schema. As stated in the introduction, the main focus chosen for this thesis is to present an overview of REE distribution in the Lower Ordovician complexes. Thus, the primary information about rock complexes, their mineralogy, major elements and the REE contents are presented in the following sections. A summarising graph of the results can be found in Appendix 1.

4.1. Mineralogy of Studied Lithologies

The average semi-quantitative mineral composition of the samples obtained based on XRD Rietveld refinement is presented visually on column charts (Figure 15, Figure 16) and a depth profile (Figure 25). The mineralogy of each sample complex is given according to XRD results with related standard deviations. After an overall description of the mineralogy of the rock complexes, all rock types are analysed in detail below.

4.1.1. Average Mineralogy

Figure 15 and Figure 16 give an overview of the mineralogy of studied complexes. The highest levels of **dolomite** ($CaMg(CO_3)_2$) can be detected in limestone (40%) and glauconitic sandstone (13%); the highest levels of **calcite** ($CaCO_3$) are associated with limestone (45%); the highest content of **feldspars** can be found in mudstones (51%) and glauconitic sandstones (13%); maximum **quartz** (SiO_2) content appears in phosphorite (75%), glauconitic sandstone (28%) and mudstone (26%); the highest **pyrite** (FeS_2) concentrations can be detected in phosphorite (2%). Concerning clay minerals, the maximum **chlorite** ($(Mg,Fe)_3(Si,Al)_4O_{10}(OH)_2 \cdot (Mg,Fe)_3(OH)_6$), **muscovite** ($(KF)_2(Al_2O_3)_3(SiO_2)_6(H_2O)$) and/or **illite** ($(KH_3O) \cdot (Al,Mg,Fe)_2 \cdot (SiAl)_4 \cdot O_{10} \cdot [(OH)_2(H_2O)]$) levels are detected in mudstone (3% and 16%). **Glauconite** ($(K,Na)(Fe,Al,Mg)_2(Si,Al)_4O_{10}(OH)_2$) can be mostly found in glauconitic sandstone (34%). From minor phases **anatase** (TiO_2) content is the highest in mudstones (0.55%); while **zircon** ($ZrSiO_4$) can only be detected in phosphorites (0.02%). **Apatite** ($Ca_5(PO_4)$) amount peaks in phosphorite (18.90%), and locally in limestone (1.73%) and glauconitic sandstone (1.46%). **Goethite** ($FeO(OH)$) appears in limestones (1.83%). It should be noted that presented feldspars data include the merged XRD results of sanidine ($KAlSi_3O_8$) and orthoclase ($KAlSi_3O_8$), and the data of dolomites include the results of dolomite and Ca-dolomite.
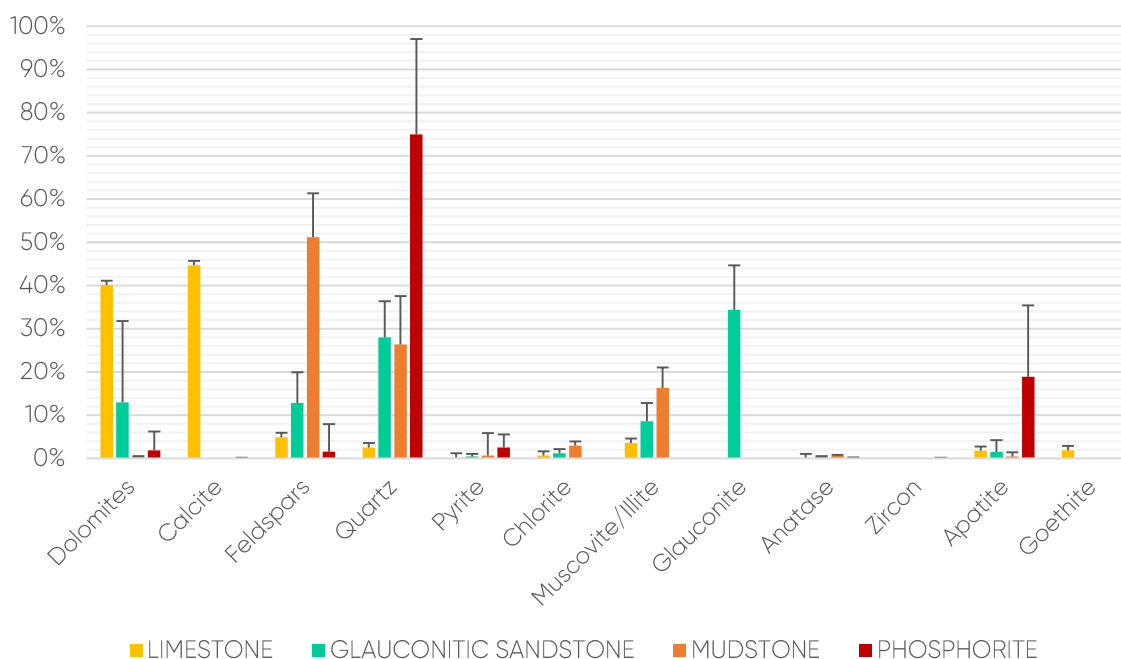
Figure 15. Average mineralogy of studied rock complexes according to XRD Rietveld analyses. The standard deviation whisker shows how widely the samples are dispersed from the mean.
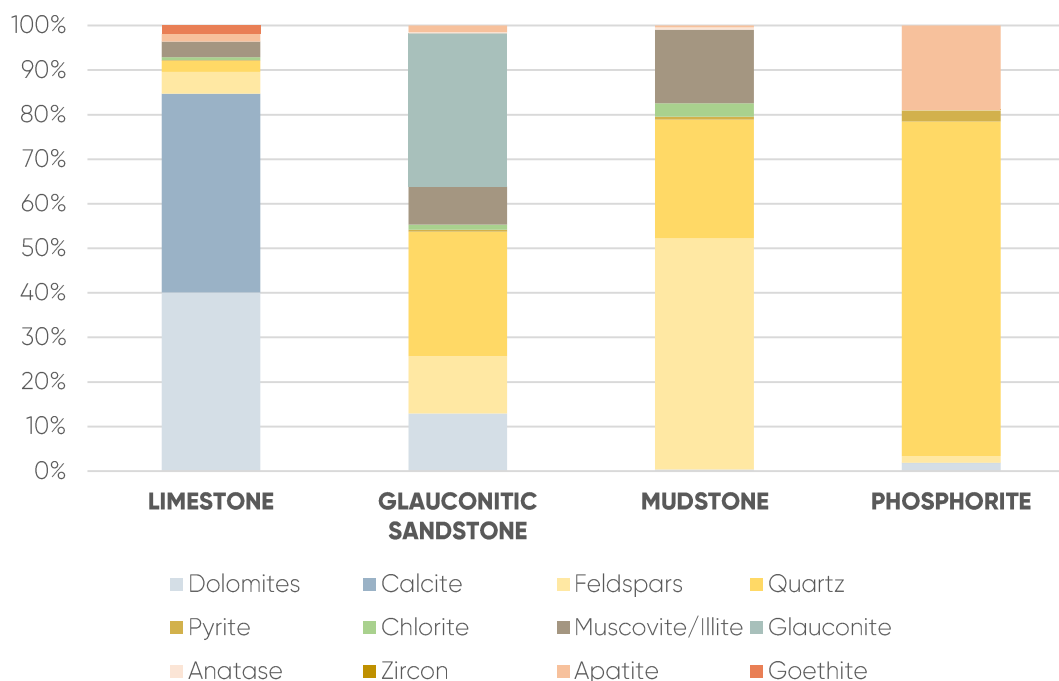
Figure 16. Average mineralogy of studied rock complexes according to XRD Rietveld analyses.

a) Limestone samples

The average main composition of limestone samples seen in Figure 16 and Figure 18 is calcite (44.65%), dolomite (40.06%), feldspars (4.87%) and muscovite/illite (3.56%). At the approximate depth of 16.75 m, the dominant mineral changes from calcite to dolomite. The first 4 samples (depths 14.50-15.08 m) show significant goethite content (average 10.25%, Figure 17).
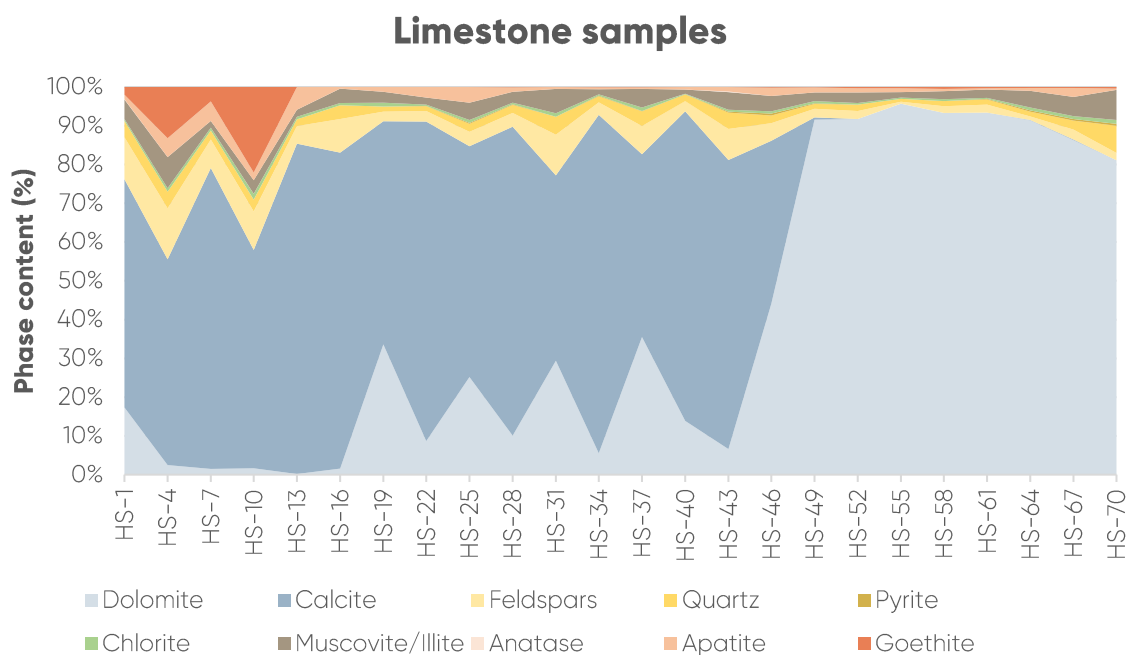
Figure 17. Limestone sample's mineralogy, the Toila Formation (n=24).
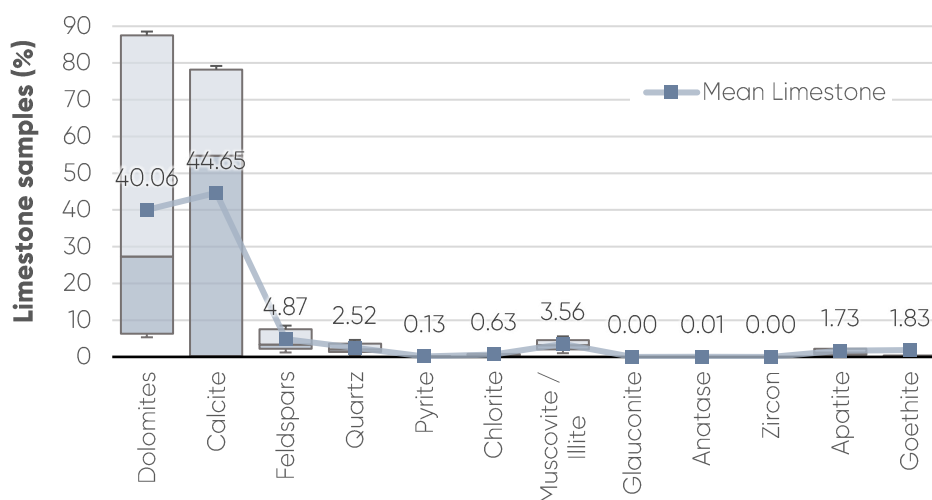
Figure 18. Mean values and standard deviation of the limestone mineral phases. The lower boundary of the box is the 1st quartile (25th percentile) the upper boundary of the box is the 3rd quartile (75th percentile), and the whisker caps' locations show the minimum and maximum values.

b) Glauconitic sandstone samples

The average composition of glauconitic sandstone samples is glauconite 34.35%, quartz 27.94%, dolomites 12.95%, feldspars 12.82% and muscovite/illite 8.59% (Figure 16, Figure 20). The upper half of the samples (depths 17.95-18.75 m) presents a high content of dolomite and the amount of glauconite generally increases with depth being the highest in the middle part of the Leetse Formation (Figure 19). Notably, in the lower part of the formation, apatite-rich intervals could be followed.
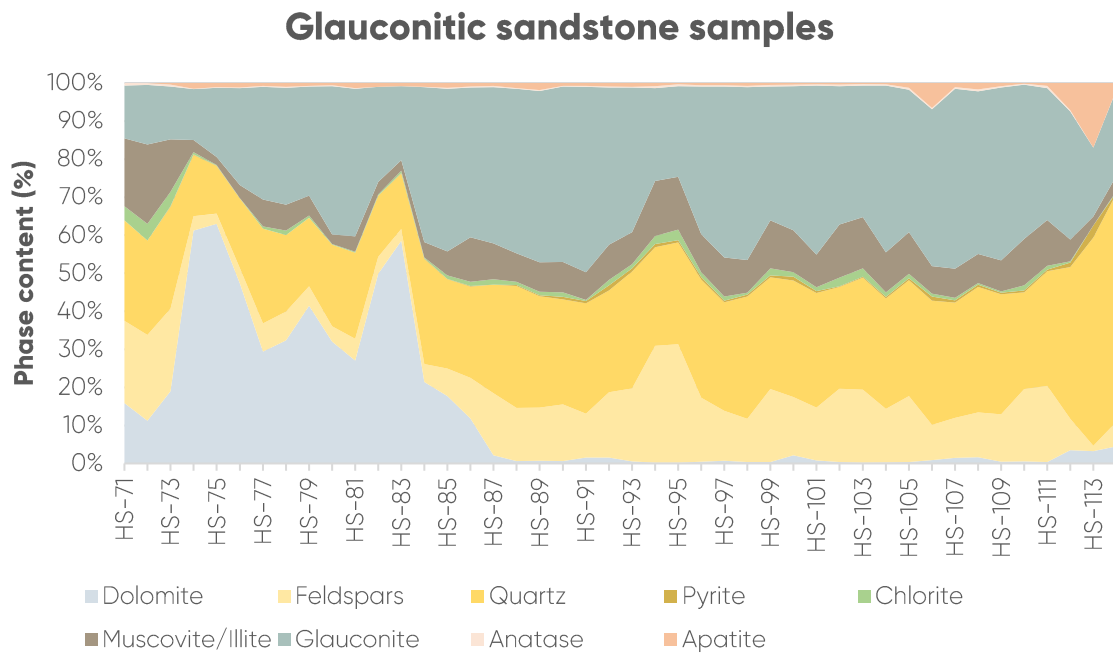
Figure 19. Glauconitic sandstone sample's mineralogy, the Leetse Formation (n=44).
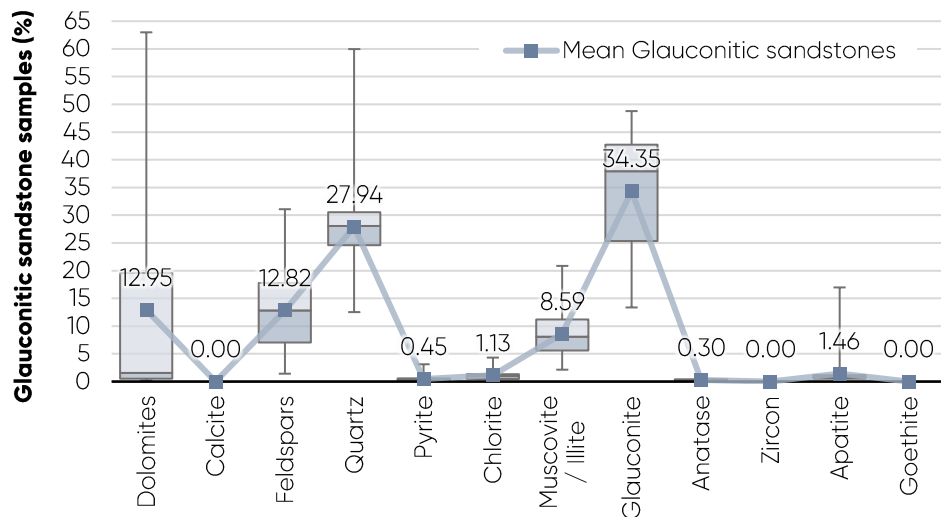
Figure 20. Mean values and standard deviation of the glauconitic sandstone mineral phases.

c) Mudstone samples

The average mineral composition of mudstone samples from the Varangu Formation is feldspars 51.19%, quartz 26.34%, and muscovite/illite 16.28% (Figure 16, Figure 22). The samples have quite similar mineralogical composition, except the last 4 samples (depths 21.30-21.55 m), where feldspars content decreases and pyrite content increases (average 13.14%, Figure 21).
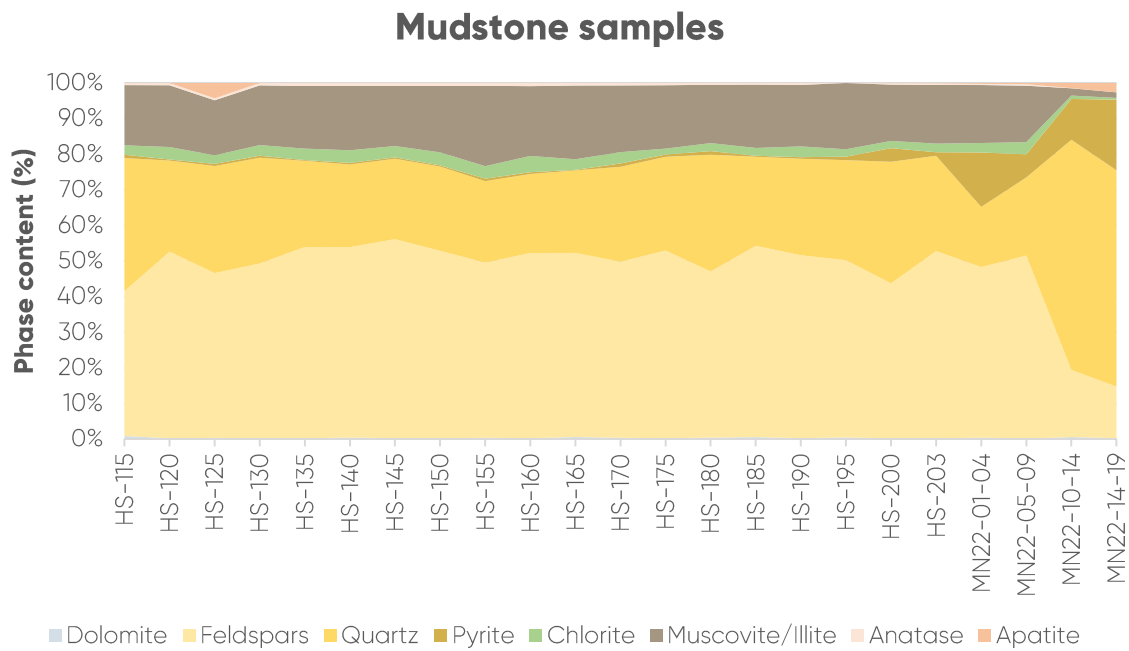
Figure 21. Mudstone sample's mineralogy, the Varangu Formation (n=23).
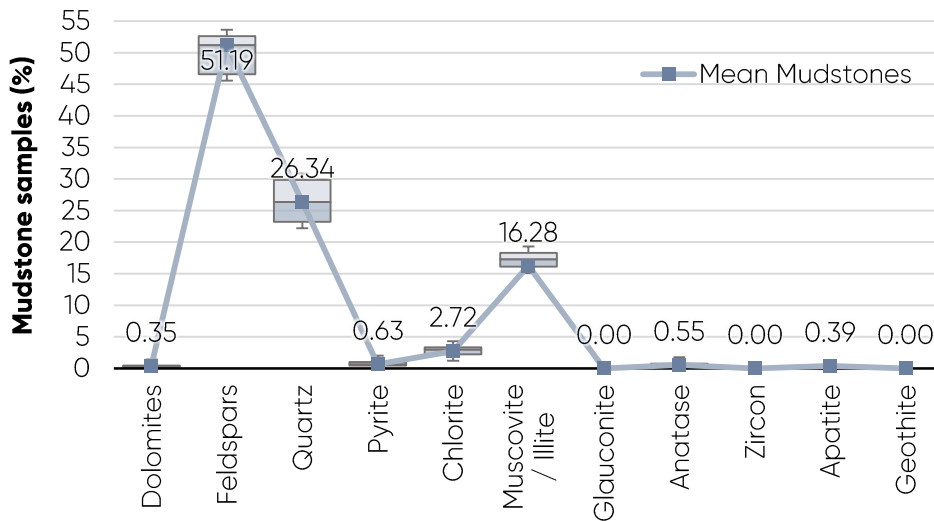
Figure 22. Mean values and standard deviation of the mudstone mineral phases.

d) Phosphorite samples

The average mineral composition of phosphorite samples from the Kallavere Formation are quartz 74.98%, apatite 18.90%, and pyrite 2.50% (Figure 16, Figure 24). The samples in depths 23.65-24.15 m and 24.75-25.15 m have higher values of apatite (Figure 23). The lower part of the studied profile also presents a notable proportion of dolomite.
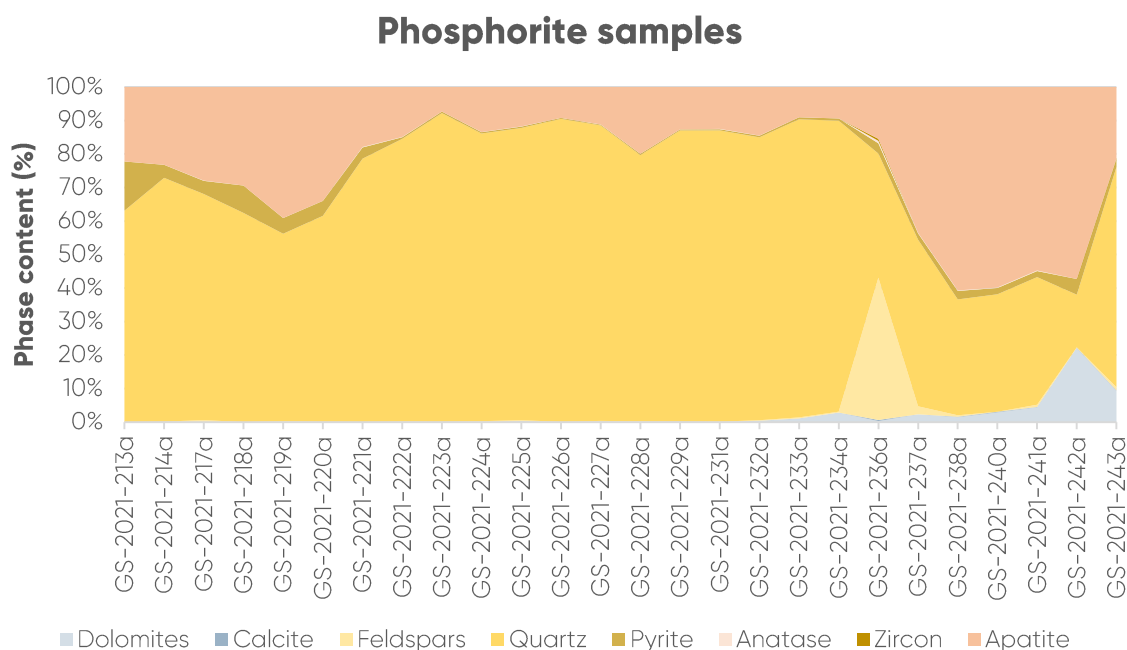
Figure 23. Phosphorite sample's mineralogy, the Kallavere Formation (n=26).
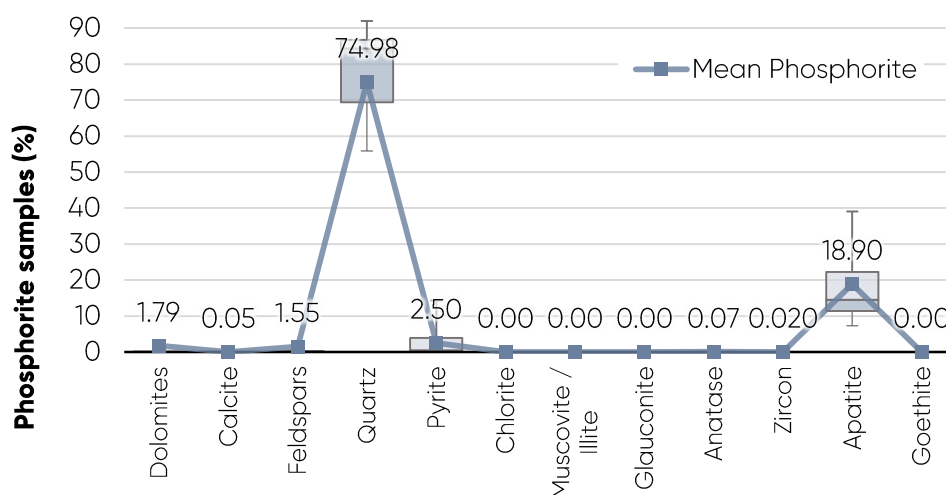
Figure 24. Mean values and standard deviation of the phosphorite mineral phases.

4.1.2. Mineral Composition Depth Model

To visually present the mineralogical variation, a mineralogy depth model of 5 cm resolution was created for the depths of 14.50-25.20 metres (Figure 25). Some rock complexes had lower resolution data available, but to achieve a 5 cm resolution model, related data were interpolated between the samples by averaging. The average mineralogy of rock complexes has been described in paragraph 4.1.1.
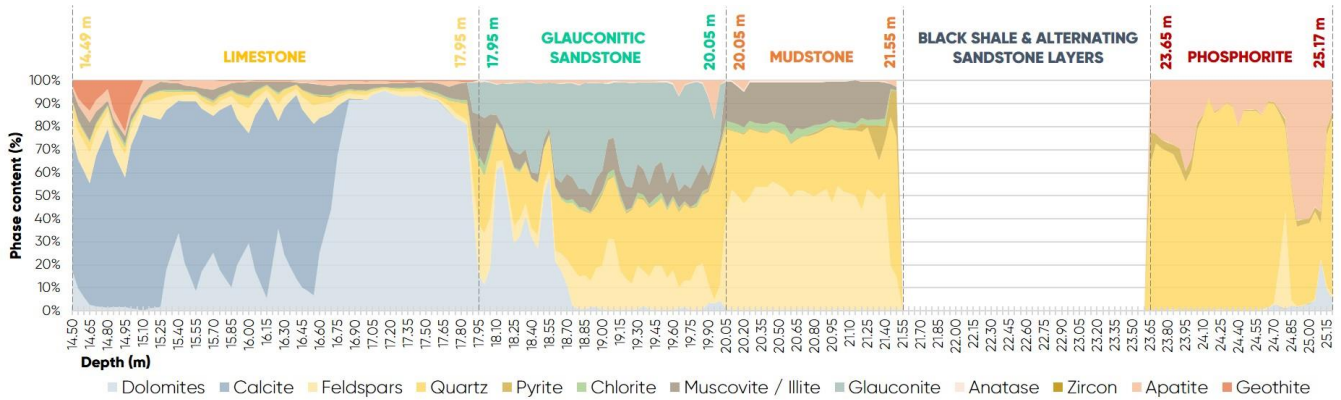
Figure 25. Mineral composition model (resolution 5 cm) for the studied drill core profile based on XRD Rietveld analyses.

4.2. Major Elements of the Complexes

The XRF disc analysis results in Figure 26 describe the distribution of the major elements in the samples. In the composition of **limestones** CaO (35.48%), SiO_2 (10.10%) and MgO (7.40%) dominate; in **glauconitic sandstones** SiO_2 (56.14%), Al_2O_3 (9.78%), Fe_2O_3 (9.32%), and K_2O (5.92%) are present via major compounds; in **mudstones** SiO_2 (63.28%), Al_2O_3 (15.41%), K_2O (8.89%), and Fe_2O_3 (3.63%) occur via major elements; and in **phosphorites** SiO_2 (64.88%), CaO (15.32%), and P_2O_5 (10.08%) appear as dominant compounds.
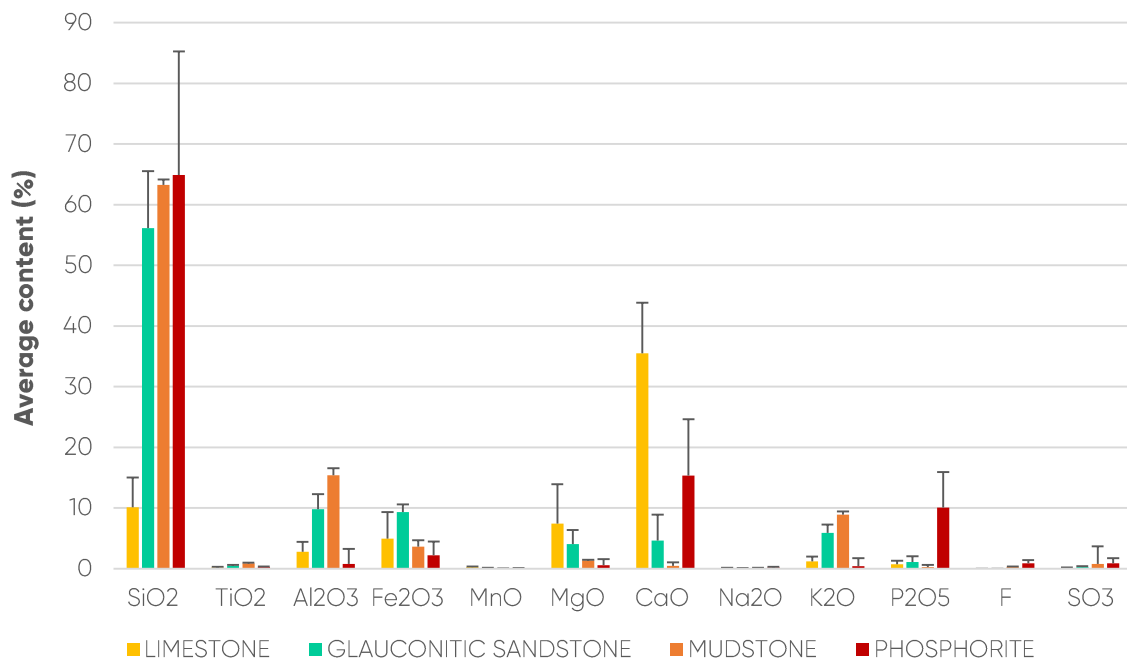
Figure 26. The major components average content of the studied rock complexes based on XRF analyses.

To create a major components model of the studied lithologies, 6 major elements (Al_2O_3, Fe_2O_3, MnO, CaO, P_2O_5 and SO_3) were chosen (Figure 27). **Al_2O_3** content is generally high in the whole mudstone section (20.05-21.55 m) but also peaks at the boundary of limestone and glauconitic

34

sandstone complexes (depth 17.95 m). **Fe₂O₃** concentration is the highest in the uppermost limestone samples (depths 14.65 m and 14.95 m). **MnO** content remains low compared to other elements, but shows higher values in the limestone horizons (depths 16.70-17.90 m). **CaO** peaks in the calcite-rich section of the limestone of the Toila Formation. **P₂O₅** has larger peaks at 19.90 m in the glauconitic sandstone region and shows elevated concentration throughout the phosphorite horizon (23.65-25.17 m – larger peaks at 23.95 m, 24.40 m, and in the range 24.90-25.10 m). Smaller peaks of P₂O₅ can be detected at 14.50-14.95 m, 15.10 m, 15.70 m, 16.65 m and 17.70 m for limestone horizons, and 20.20 m and 21.50 for mudstone samples. **SO₃** content peaks at 21.50 m above black shale complexes and presents higher values also in phosphorites.
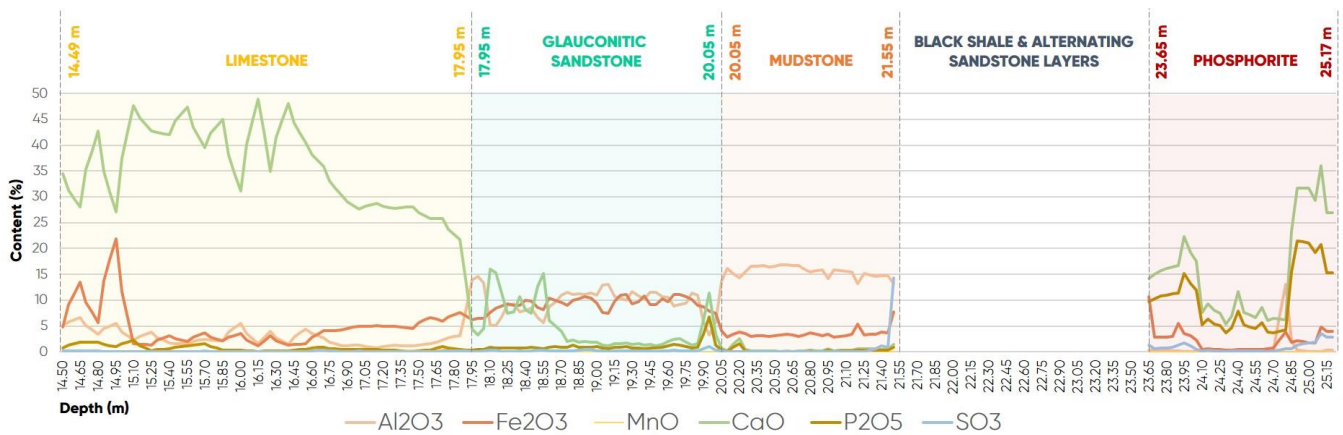
Figure 27. Major components model (resolution 5 cm) for the studied drill core profile based on XRF disk analyses.

4.3. Rare Earth Elements Distribution

The average REE content of the samples obtained based on ICP-MS data is presented and visualised in the following subchapters.

4.3.1. Average REE Content

Figure 28 provides an overview of REE distribution in all the rock complexes; the highest value of each REE can be found in phosphorite. The total REE content is on average 95±2 ppm for **limestones**, 142±2 ppm for **glauconitic sandstones**, 157±6 ppm for **mudstones** and 1026±23 ppm for **phosphorites**. All rock complexes are described separately below.
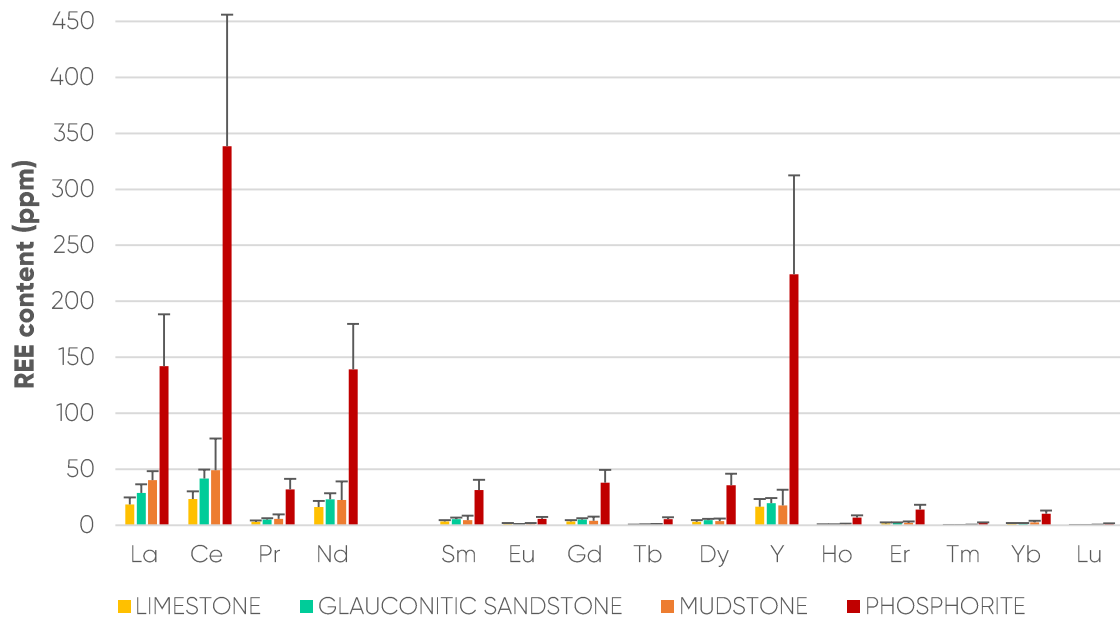
Figure 28. The average content of REEs in studied rock complexes based on ICP-MS analyses.

When the average REE values of all the rock complexes are compiled, Ce, Y, La, and Nd appear as the most enriched elements (Figure 29). Based on the figure, the sum of **light rare earth elements (LREE)** (La, Ce, Pr, Nd) in all the complexes is 929.23 ppm, **medium rare earth elements (MREE)** (Sm, Eu, Gd, Tb, Dy) is 161.07 ppm, and **heavy rare earth elements (HREE)** (Ho, Er, Tm, Yb, Lu) is 51.54 ppm.
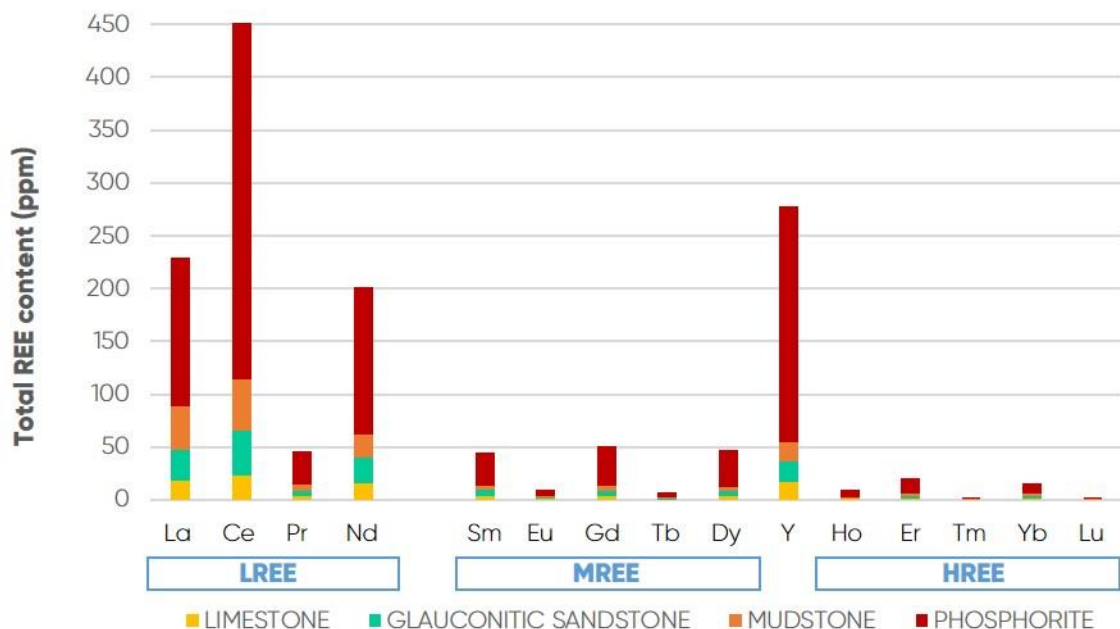
Figure 29. Total REE content by elements and rock complexes. The division of REEs into light REE (LREE), medium REE (MREE) and heavy REE (HREE) is presented.

a) Limestone samples

As shown in Figure 30, limestones have considerably higher values of Ce, La, Y and Nd compared to other REEs, while those elements also show higher variability and standard deviation.
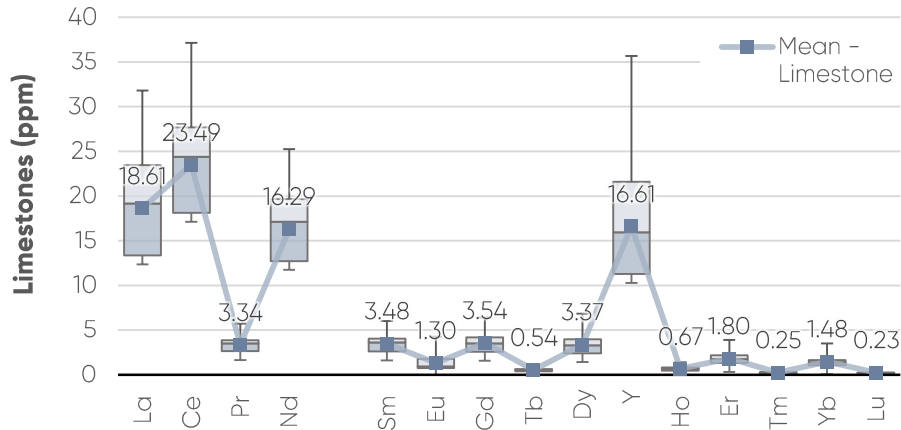
Figure 30. Mean values and standard deviation of REEs in limestone.

b) Glauconitic sandstone samples

The glauconitic sandstone samples also have higher content values of Ce, La, Nd and Y (Figure 31).
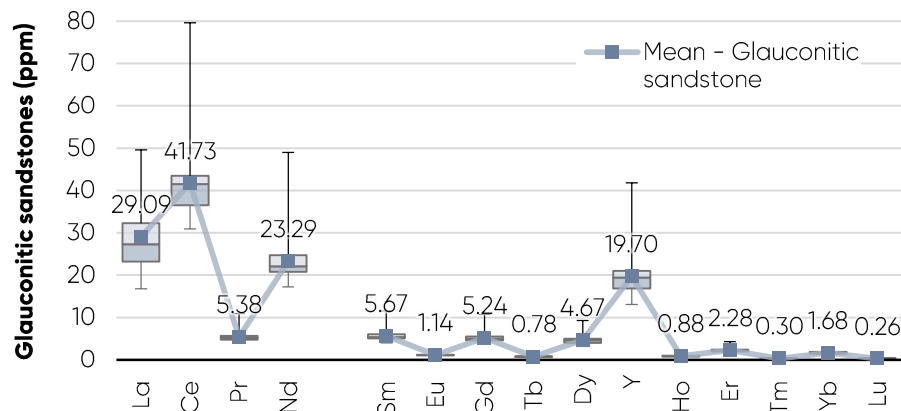
Figure 31. Mean values and standard deviation of REEs in glauconitic sandstone.

c) Mudstone samples

The mudstone samples show the highest content of Ce, La, Nd, and Y among REEs (Figure 32). For these elements, the standard deviation is also higher.
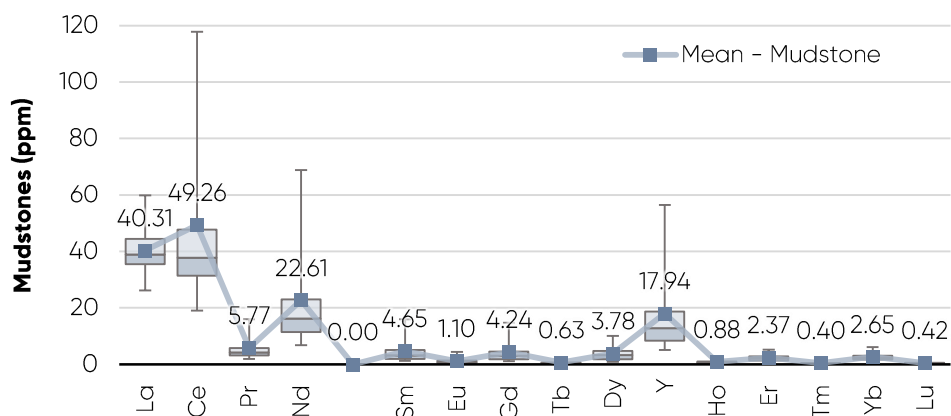
Figure 32. Mean values and standard deviation of REEs in mudstone.

d) Phosphorite samples

The enrichment pattern with Ce, Y, La and Nd as the most enriched REE is also repeated in the case of phosphorite samples (Figure 33).
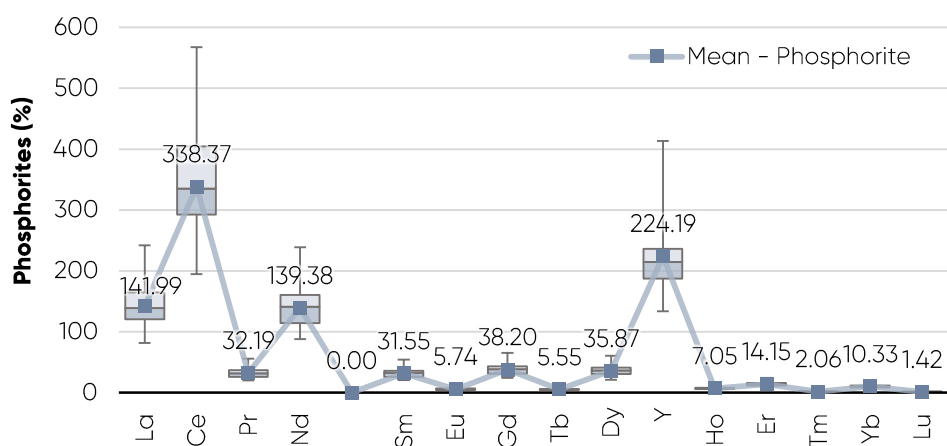
Figure 33. Mean values and standard deviation of REEs in phosphorite.

4.3.2. REE Content and Model of the Drill Core

To provide an overview of the REE distribution variability in the studied proportion of the drill core, the same depth model described earlier in paragraph 4.1.2 was used. Peak concentrations of REEs can be detected in Figure 34 at depths of 17.95 m, 19.90 m, and 20.20 m, but highest REE values are detected from 21.25 m to the end of phosphorite samples at 25.17 m. The model in the logarithmic scale in Figure 35 shows that the REEs act quite similarly in the whole section. Peaks of individual elements appear at depths of 16.70 m, 18.00 m, 19.95 m, 20.20 m, 21.40 m, and in the phosphorite region of 23.65-25.17 m. The minimum REE values appear at depths 16.15 m, 16.40 m, 16.85 m, 20.05 m, 20.30 m, and 24.80 m. Figure 36 illustrates the sum of REE content by 5 cm resolution. Peaks of REE can be seen at depths of 19.90 m, 19.95 m, and 20.20 m. The amounts of REE start to rise from 21.30 m to the phosphorite samples, declining at 24.80 m and peaking at their maximum at 25.05 metres.
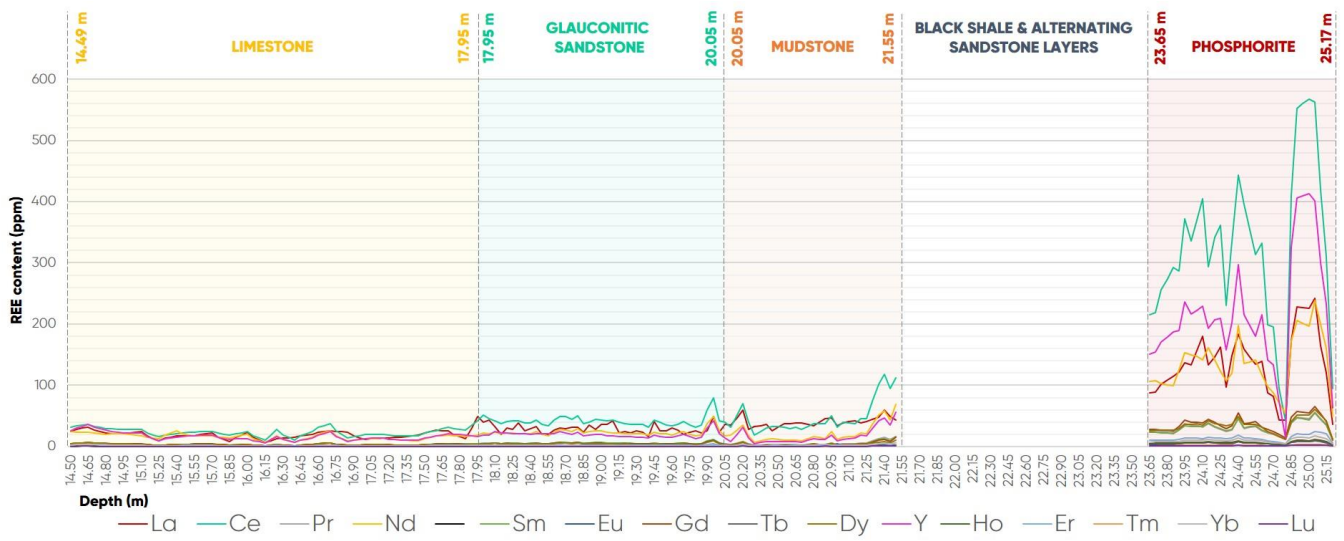
Figure 34. REE distribution model in the Aseri PH012B drill core.
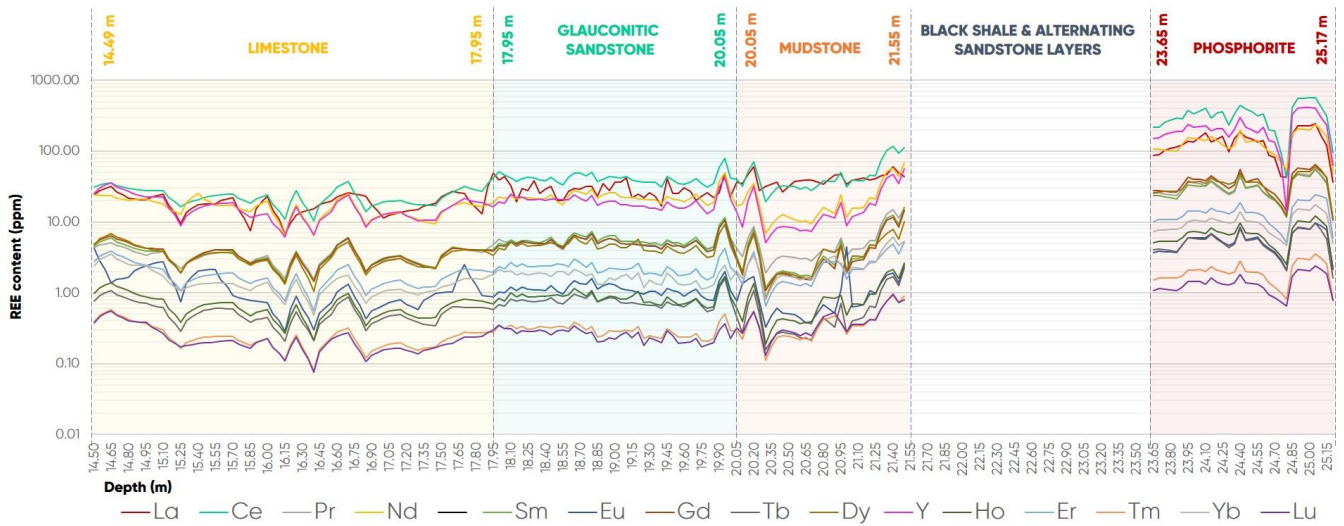
Figure 35. REE distribution model in the Aseri PH012B drill core (logarithmic scale).
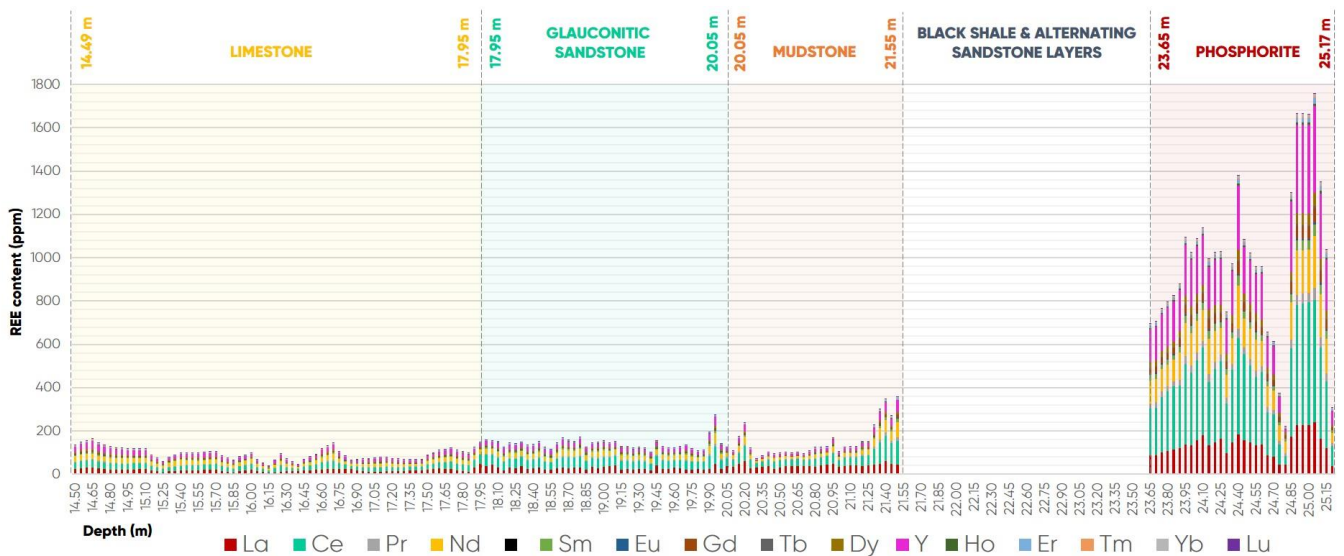
Figure 36. The sum of REE content in the Aseri PH012B drill core.

4.3.3. REE Normalised Patterns

To characterise REE distribution in sedimentary rocks, normalised values are commonly used to indicate enrichment or depletion respect to standard compilations, such as PAAS - Average Post-Archean Australian Shale, employed in this thesis (Taylor & McLennan, 1985). The normalised values are calculated by dividing the original values by those from the standard data sets. This method also helps to eliminate the 'zig-zag' patterns seen in non-normalised REE distribution graphs, occurring due to the Oddo-Harkins effect – where rare earth elements with even atomic numbers are more abundant than their odd-numbered neighbours and the lighter REE are predominant due to their larger ionic radii (Harkins, 1917).

The normalised REE patterns for the studied limestone, glauconitic sandstone, and mudstone suggest that the enrichment levels of these complexes are similar to that of average shale (values of Figure 37, Figure 38 and Figure 39 cluster around 1). However, in the case of phosphorite, some REEs show up to ten-fold enrichment (Figure 40). Limestone samples exhibit a pronounced negative Ce anomaly and a strong positive Eu anomaly. Glauconitic sandstone samples show a strong negative anomaly for both Ce and Y. Mudstone samples display strong positive Eu peaks in certain instances, and the maximum REE values of mudstones are related to the Varangu Formation. The lowermost samples (21.35 to 21.50) display a different behaviour, with an enrichment of up to 3-fold and an MREE bulge (Figure 39). Additionally, some phosphorite samples present a negative anomaly of Ce and Y. Despite the varying enrichment levels, a common feature of the limestones, glauconitic sandstones, and phosphorite is MREE enrichment (Figure 41).
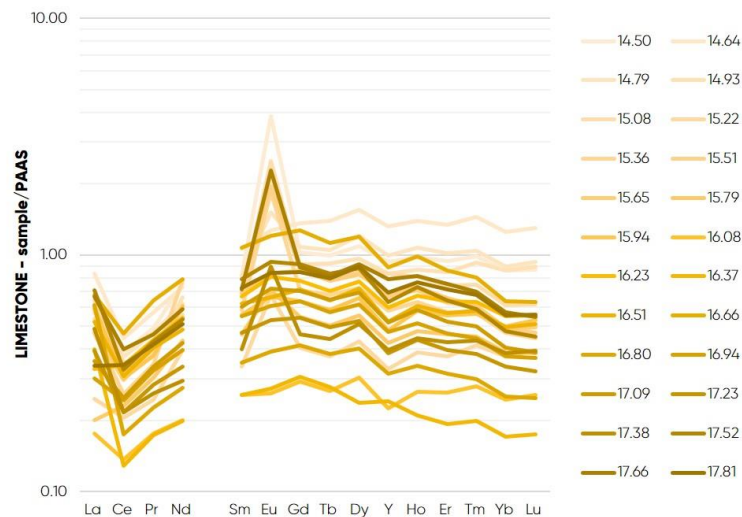
Figure 37. PAAS normalised REE distribution in the Aseri PH012B core for limestone samples.
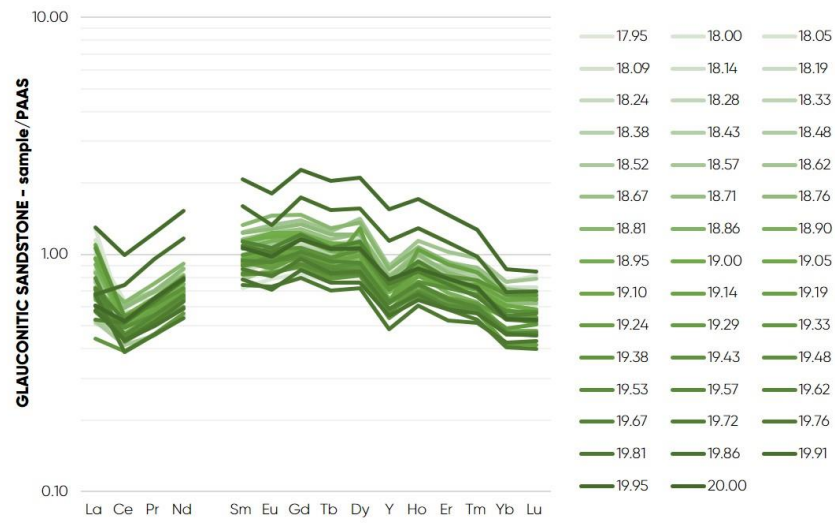
Figure 38. PAAS normalised REE distribution in the the Aseri PH012B core for glauconitic sandstone samples.
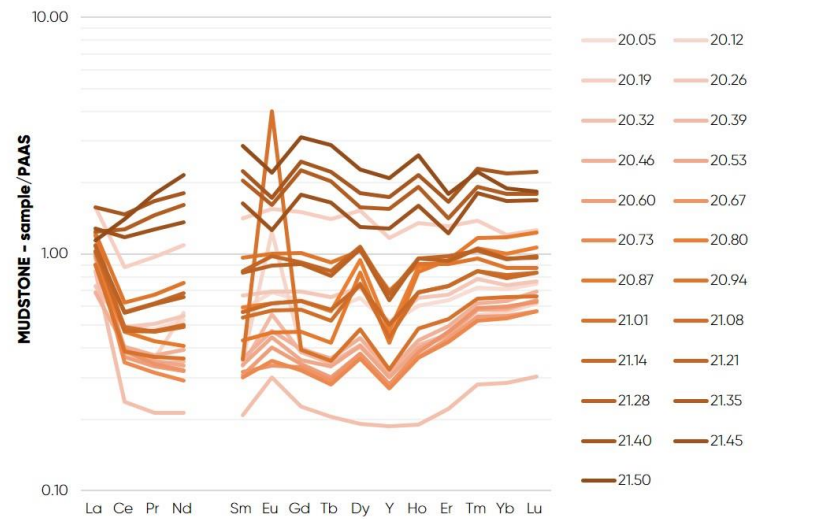
Figure 39. PAAS normalised REE distribution in the Aseri PH012B core for mudstone samples.
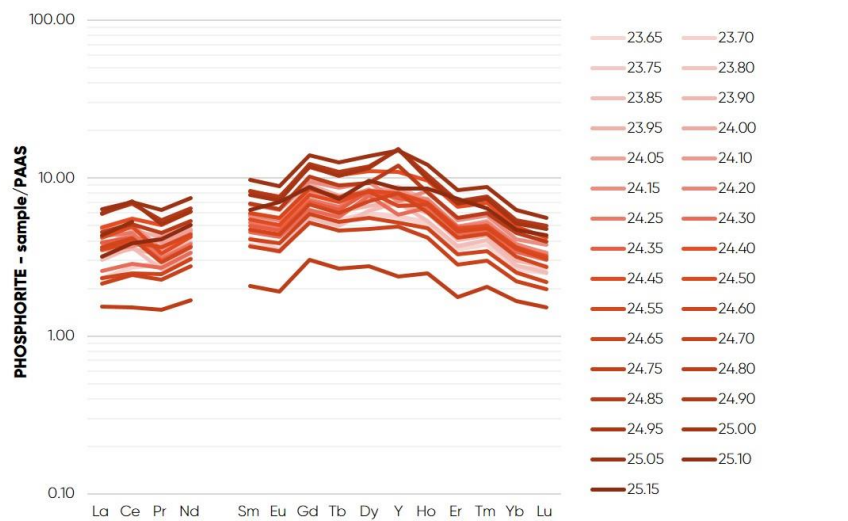
Figure 40. PAAS normalised REE distribution in the Aseri PH012B core for phosphorite samples.
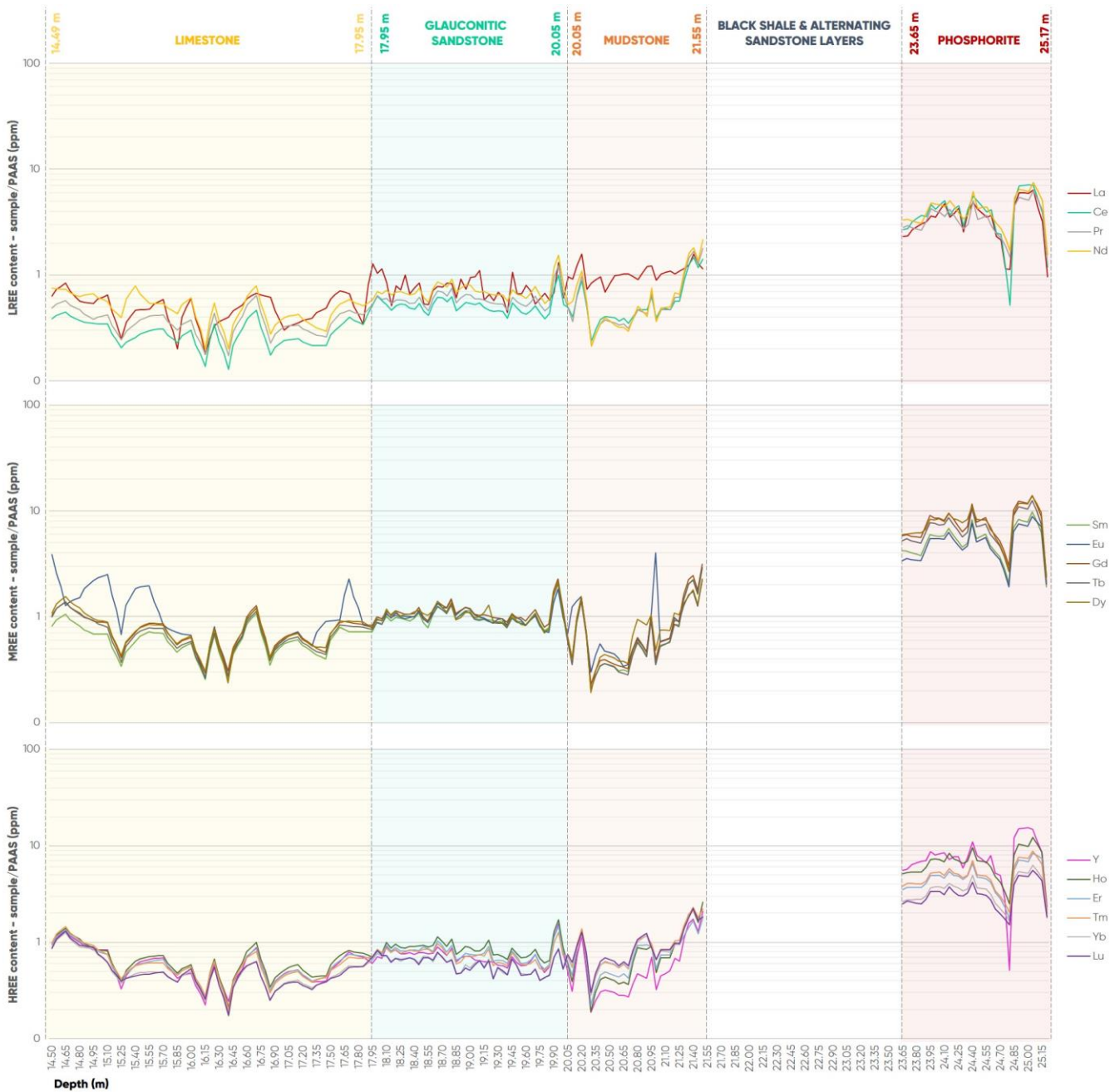
Figure 41. Overall PAAS normalised REE distribution model by LREE, MREE, HREE in the Aseri PH012B drill core.

5. Discussion

This section of the thesis will be used to discuss the results of the thesis and use them to make further conclusions about the distribution of REE in Estonian Lower Ordovician complexes. To summarise some of the key results – on average, the highest total values of REE can be found in phosphorite, after that in mudstones, and glauconitic sandstones, while limestones have the lowest content of REEs. The greatest proportion of the REEs in the rock complexes comprises of the LREEs, then MREEs and the lowest amount is the HREEs. The normalised REE patterns for the studied limestone, glauconitic sandstone, and mudstone suggest that the general enrichment levels of these complexes are similar to that of average shale (PAAS normalisation). However, in the case of phosphorite, REEs show up to ten-fold enrichment.

5.1.1. Comparison of the Results to Reference Data from Estonia

When comparing the results obtained in this thesis to the reference data provided by Kiipli et al. (2000) as shown in Figure 42, which includes limestone, dolomite, mudstone, and black shale samples used for calibration and control in various analyses over the years, several observations can be made. The closest reference samples to those analysed in this thesis are Es-3 for limestone (Väo Formation, Middle Ordovician), Es-16 for dolomite (Kunda Stage, Middle Ordovician), and Es-1 for mudstone (Lontova Stage, Early Cambrian). Notably, the limestone and mudstone samples exhibit significant differences in REE enrichment magnitude. All reference limestone and dolomite samples fall below the 1-fold value line and thus relative REE depletion, whereas the thesis results show a strong positive anomaly for Eu and a general enrichment. Both the reference and thesis data display lower Ce and Tb values than neighbouring elements. The reference data of carbonate rocks indicate a peak for Y, which is not observed in the thesis samples. While the overall pattern is similar, the thesis data offers higher resolution and includes more detailed sample patterns. The reference mudstone sample shows REE enrichment above the 1-fold value line; however, mudstone samples from the Varangu Formation analysed in the thesis exhibit a wide enrichment range, with at least half of the samples showing values below the 1-fold line.
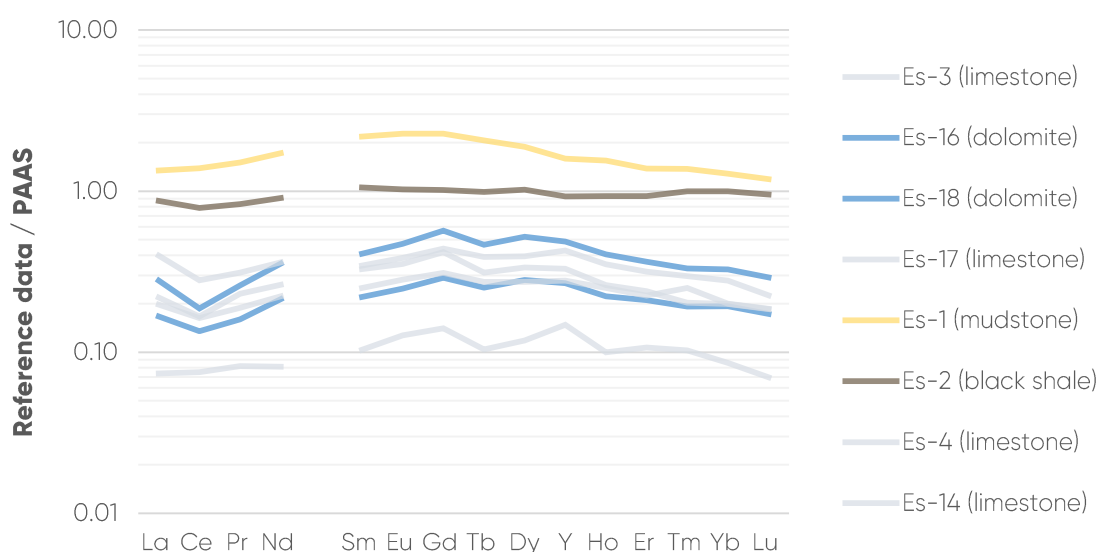
Figure 42. Average shale-normalised REE reference data from Estonia (Kiipli et al., 2000).

5.1.2. REE Behaviour and Enrichment

To assess the REE pairwise relationships with different components, Pearson correlation coefficients (R) for REEs and selected components are calculated for each rock complex. Compared datasets include the REEs, major mineral components, and Zr and MnO, which can enrich together with the REEs. The correlation between MnO and REE enrichment has been observed by Graul, Kallaste, Pajusaar, et al. (2023).

As presented in Table 2, the limestones of the Toila Formation show a strong positive correlation between most of the REEs (≥ 0.80), except for Eu and La, which have medium or low correlation with other elements (0.41 to 0.57). Calcite and dolomite show none or very weak to moderate negative correlation respectively to each other (-0.95), and with REEs (-0.10 to -0.45). Apatite presents a good correlation with all REE (≥ 0.55), except Eu (≥0.22). With calcite, there is almost no correlation. It can be concluded that calcite formation did not have major control on REE accumulation in primary sediments. Feldspars and Zr seem to present an increasing covariance with HREE. As there is also a strong correlation between the abundance of quartz, feldspars, clays and Zr (≥ 0.70), which make up detrital admixture in limestones, the measured REE signal is likely partly inherited from terrigenous fraction and thus dependent on source, weathering and sediment sorting during transport (Bayon et al., 2015). Nevertheless, the REEs also show a similar moderately to strong positive correlation with seaborne detrital compounds, such as goethite (0.24 to 0.72) and apatite (0.27 to 0.74).

Table 2. Pearson correlation coefficients of REEs, main mineral phases and selected minor elements in limestones.

LIMESTONE SAMPLES (n=24)																							
	La	Ce	Pr	Nd	Sm	Eu	Gd	Tb	Dy	Y	Ho	Er	Tm	Yb	Lu	Calcite	Quartz	Apatite	Geothite	∑Dolomite	∑Feldspar	∑Clay	Zr	MnO
La	1.00																							
Ce	0.75	1.00																						
Pr	0.73	0.99	1.00																					
Nd	0.64	0.89	0.87	1.00																				
Sm	0.76	0.97	0.98	0.86	1.00																			
Eu	0.41	0.55	0.50	0.67	0.49	1.00																		
Gd	0.77	0.97	0.97	0.86	0.99	0.52	1.00																	
Tb	0.78	0.95	0.94	0.85	0.97	0.53	0.99	1.00																
Dy	0.77	0.95	0.94	0.84	0.97	0.52	0.99	1.00	1.00															
Y	0.77	0.92	0.90	0.82	0.93	0.58	0.96	0.98	0.99	1.00														
Ho	0.77	0.94	0.92	0.84	0.95	0.54	0.98	0.99	1.00	0.99	1.00													
Er	0.76	0.93	0.89	0.83	0.92	0.55	0.96	0.98	0.99	0.99	1.00	1.00												
Tm	0.73	0.89	0.85	0.80	0.88	0.54	0.92	0.96	0.97	0.98	0.99	0.99	1.00											
Yb	0.71	0.87	0.81	0.78	0.85	0.55	0.90	0.94	0.95	0.97	0.97	0.98	1.00	1.00										
Lu	0.70	0.86	0.80	0.76	0.83	0.53	0.88	0.92	0.94	0.96	0.96	0.98	0.99	1.00	1.00									
Calcite	-0.10	0.10	0.08	0.19	0.02	0.26	0.08	0.09	0.10	0.16	0.13	0.15	0.18	0.19	0.20	1.00								
Quartz	0.35	0.54	0.48	0.51	0.41	0.32	0.43	0.46	0.48	0.49	0.51	0.55	0.60	0.63	0.65	0.36	1.00							
Apatite	0.59	0.58	0.56	0.44	0.60	0.27	0.66	0.67	0.69	0.74	0.70	0.69	0.68	0.64	0.65	0.33	0.12	1.00						
Geothite	0.42	0.46	0.36	0.41	0.44	0.24	0.51	0.58	0.57	0.61	0.60	0.63	0.68	0.71	0.72	0.08	0.39	0.40	1.00					
∑Dolomite	-0.10	-0.32	-0.27	-0.37	-0.23	-0.34	-0.29	-0.32	-0.33	-0.40	-0.37	-0.40	-0.44	-0.45	-0.47	-0.95	-0.56	-0.45	-0.35	1.00				
∑Feldspar	0.48	0.64	0.55	0.60	0.52	0.44	0.57	0.62	0.64	0.67	0.68	0.72	0.77	0.80	0.82	0.39	0.94	0.33	0.60	-0.63	1.00			
∑Clay	0.63	0.71	0.68	0.67	0.66	0.22	0.66	0.69	0.70	0.68	0.71	0.72	0.74	0.74	0.75	0.04	0.81	0.28	0.51	-0.30	0.80	1.00		
Zr	0.51	0.66	0.58	0.60	0.57	0.36	0.61	0.67	0.69	0.71	0.72	0.76	0.81	0.84	0.86	0.27	0.89	0.34	0.74	-0.55	0.97	0.84	1.00	
MnO	0.41	0.40	0.38	0.35	0.41	0.31	0.44	0.48	0.49	0.51	0.50	0.52	0.54	0.55	0.55	0.05	0.41	0.26	0.34	-0.21	0.49	0.48	0.49	1.00

Regarding glauconitic sandstones, there is a strong positive correlation between most REEs (≥0.70), except La, which shows a low covariance (∼0.35) (Table 3). No correlation to strong negative correlation was detected between glauconite and all REEs (0 to -0.61). Quartz, dolomite, and glauconite exhibit negative correlations with each other (∼0 to -0.65). Feldspar, clays and Zr are positively related. MnO presents a strong positive correlation with dolomite (0.98), and to a lesser extent, with HREE (0.10 to 0.50). Notably, a strong positive correlation between apatite and REEs suggests that REE capture in glauconitic sandstones is most likely connected to apatite distribution. The lower correlation between apatite and La, and the moderate positive correlation of La with clay phases, can be connected to specific behaviour of La in marine environments (Abbott et al., 2019; Grenier et al., 2018).

Table 3. Pearson correlation coefficients of REEs, main mineral phases and selected minor elements in glauconitic sandstones.

GLAUCONITIC SANDSTONE SAMPLES (n=44)																						
	La	Ce	Pr	Nd	Sm	Eu	Gd	Tb	Dy	Y	Ho	Er	Tm	Yb	Lu	Quartz	Glauconite	Apatite	∑Dolomite	∑Feldspar	∑Clay	Zr	MnO
La	1.00																						
Ce	0.58	1.00																					
Pr	0.43	0.97	1.00																				
Nd	0.36	0.94	0.99	1.00																			
Sm	0.29	0.90	0.97	0.99	1.00																		
Eu	0.35	0.86	0.89	0.90	0.93	1.00																	
Gd	0.30	0.91	0.97	0.98	0.99	0.94	1.00																
Tb	0.29	0.90	0.96	0.97	0.99	0.94	1.00	1.00															
Dy	0.27	0.86	0.90	0.91	0.93	0.90	0.94	0.95	1.00														
Y	0.33	0.88	0.89	0.89	0.89	0.84	0.92	0.94	0.93	1.00													
Ho	0.30	0.87	0.89	0.89	0.90	0.87	0.92	0.94	0.99	0.95	1.00												
Er	0.33	0.85	0.84	0.83	0.83	0.82	0.86	0.89	0.96	0.95	0.98	1.00											
Tm	0.41	0.81	0.75	0.72	0.72	0.75	0.76	0.79	0.89	0.89	0.92	0.97	1.00										
Yb	0.49	0.67	0.53	0.47	0.46	0.55	0.51	0.55	0.67	0.70	0.73	0.83	0.93	1.00									
Lu	0.53	0.66	0.50	0.43	0.41	0.50	0.46	0.49	0.61	0.66	0.67	0.78	0.89	0.98	1.00								
Quartz	0.11	0.44	0.55	0.57	0.53	0.31	0.48	0.44	0.33	0.30	0.29	0.20	0.06	-0.18	-0.18	1.00							
Glauconite	-0.44	-0.26	-0.11	-0.04	0.05	0.04	0.00	-0.05	-0.08	-0.31	-0.17	-0.31	-0.44	-0.58	-0.61	0.14	1.00						
Apatite	0.29	0.75	0.83	0.84	0.81	0.65	0.81	0.82	0.75	0.81	0.75	0.70	0.59	0.33	0.30	0.55	-0.16	1.00					
∑Dolomite	-0.08	-0.10	-0.19	-0.20	-0.17	-0.05	-0.10	-0.02	0.08	0.25	0.14	0.27	0.38	0.49	0.48	-0.65	-0.56	-0.09	1.00				
∑Feldspar	0.32	-0.15	-0.21	-0.26	-0.32	-0.30	-0.37	-0.42	-0.45	-0.54	-0.47	-0.48	-0.44	-0.28	-0.25	0.07	0.02	-0.35	-0.62	1.00			
∑Clay	0.40	-0.07	-0.20	-0.28	-0.37	-0.35	-0.40	-0.45	-0.45	-0.49	-0.43	-0.40	-0.32	-0.10	-0.03	0.01	-0.11	-0.35	-0.50	0.88	1.00		
Zr	0.23	0.08	0.04	0.01	-0.03	-0.05	-0.08	-0.12	-0.20	-0.28	-0.21	-0.24	-0.22	-0.14	-0.08	0.31	0.19	-0.10	-0.65	0.63	0.64	1.00	
MnO	-0.02	-0.06	-0.16	-0.18	-0.17	-0.06	-0.10	-0.02	0.07	0.26	0.14	0.27	0.38	0.50	0.50	-0.62	-0.65	-0.07	0.98	-0.55	-0.42	-0.64	1.00

In Table 4, the correlation coefficients for the mudstone samples are presented. A strong positive correlation between all REEs (~0.95), except La which has a weaker correlation (~0.70), is observed. REEs show a moderately strong correlation with apatite and quartz, except Eu, which presents weak covariance with apatite distribution. There is a negative correlation between the REEs and feldspars, clay minerals and MnO (~ -0.70). Almost no correlation between Zr and REE distribution could be detected. Considering that the REE enrichment is statistically connected to quartz and apatite, apatite is likely the main carrier phase of REEs. It has to be noted that Eu presents slightly less negative correlation with dolomite and feldspars, compared to other REE, and is most likely connected to redox conditions due to its ability to exist in both +2 and +3 oxidation states (Bright, 2020).

Table 4. Pearson correlation coefficients of REEs, main mineral phases and selected minor elements in mudstones.

MUDSTONE SAMPLES (n=23)																						
	La	Ce	Pr	Nd	Sm	Eu	Gd	Tb	Dy	Y	Ho	Er	Tm	Yb	Lu	Quartz	Apatite	∑Dolomite	∑Feldspar	∑Clay	Zr	MnO
La	1.00																					
Ce	0.72	1.00																				
Pr	0.69	1.00	1.00																			
Nd	0.66	0.98	0.99	1.00																		
Sm	0.66	0.98	0.99	0.99	1.00																	
Eu	0.26	0.44	0.46	0.47	0.46	1.00																
Gd	0.66	0.98	0.99	1.00	1.00	0.46	1.00															
Tb	0.65	0.98	0.99	0.99	1.00	0.46	1.00	1.00														
Dy	0.70	0.93	0.94	0.95	0.96	0.43	0.96	0.96	1.00													
Y	0.69	0.98	0.99	0.99	1.00	0.46	1.00	1.00	0.96	1.00												
Ho	0.68	0.97	0.98	0.98	0.99	0.45	0.99	0.99	0.98	0.99	1.00											
Er	0.74	0.94	0.94	0.94	0.95	0.42	0.94	0.94	0.99	0.95	0.98	1.00										
Tm	0.73	0.97	0.97	0.96	0.96	0.42	0.96	0.95	0.96	0.96	0.98	0.98	1.00									
Yb	0.73	0.97	0.96	0.94	0.93	0.41	0.93	0.93	0.93	0.94	0.97	0.96	1.00	1.00								
Lu	0.74	0.96	0.95	0.92	0.92	0.39	0.92	0.92	0.92	0.93	0.96	0.96	0.99	1.00	1.00							
Quartz	0.20	0.47	0.49	0.51	0.52	0.23	0.51	0.53	0.51	0.51	0.50	0.47	0.47	0.42	0.40	1.00						
Apatite	0.58	0.53	0.55	0.57	0.59	0.33	0.58	0.59	0.62	0.60	0.56	0.58	0.51	0.46	0.45	0.50	1.00					
∑Dolomite	-0.04	-0.09	-0.10	-0.11	-0.11	0.14	-0.11	-0.11	-0.15	-0.10	-0.13	-0.15	-0.13	-0.13	-0.13	0.24	-0.02	1.00				
∑Feldspar	-0.30	-0.65	-0.67	-0.69	-0.70	-0.27	-0.69	-0.70	-0.65	-0.69	-0.67	-0.61	-0.62	-0.58	-0.55	-0.94	-0.55	-0.23	1.00			
∑Clay	-0.33	-0.70	-0.72	-0.73	-0.74	-0.40	-0.74	-0.74	-0.70	-0.73	-0.73	-0.67	-0.69	-0.65	-0.63	-0.91	-0.56	-0.07	0.92	1.00		
Zr	-0.10	-0.13	-0.13	-0.17	-0.13	-0.11	-0.14	-0.14	-0.03	-0.14	-0.09	-0.01	-0.06	-0.04	-0.04	-0.20	-0.41	-0.32	0.28	0.20	1.00	
MnO	-0.46	-0.47	-0.50	-0.51	-0.54	-0.38	-0.53	-0.54	-0.68	-0.54	-0.59	-0.67	-0.57	-0.53	-0.52	-0.39	-0.47	0.29	0.36	0.55	-0.32	1.00

A strong positive correlation in phosphorites can be detected with all the REE-s (~0.98) except with La and Ce, which show slightly lower correlation coefficient values (~0.89; Table 5). The strongest correlation of REEs with other compounds appears with apatite, dolomites and MnO. All terrigenous compounds, such as quartz, clays, and feldspar, show negative relationship with REE and apatite (~ -0.42). There is almost no correlation between REEs and calcite.

Table 5. Pearson correlation coefficients of REEs, main mineral phases and selected minor elements in phosphorite samples.

	La	Ce	Pr	Nd	Sm	Eu	Gd	Tb	Dy	Y	Ho	Er	Tm	Yb	Lu	Calcite	Quartz	Apatite	∑Dolomites	∑Feldspar	Zr	MnO
La	1.00																					
Ce	0.98	1.00																				
Pr	0.87	0.89	1.00																			
Nd	0.88	0.90	1.00	1.00																		
Sm	0.89	0.90	0.99	0.99	1.00																	
Eu	0.85	0.86	0.97	0.98	0.98	1.00																
Gd	0.90	0.91	0.99	1.00	1.00	0.98	1.00															
Tb	0.91	0.91	0.99	0.99	1.00	0.97	1.00	1.00														
Dy	0.89	0.91	0.96	0.97	0.98	0.97	0.97	0.97	1.00													
Y	0.95	0.97	0.92	0.92	0.91	0.89	0.93	0.93	0.92	1.00												
Ho	0.88	0.90	0.97	0.98	0.98	0.98	0.98	0.97	1.00	0.91	1.00											
Er	0.82	0.84	0.93	0.95	0.94	0.97	0.93	0.92	0.97	0.88	0.98	1.00										
Tm	0.88	0.90	0.97	0.98	0.98	0.98	0.97	0.97	0.99	0.92	1.00	0.98	1.00									
Yb	0.88	0.89	0.96	0.98	0.97	0.98	0.97	0.97	0.99	0.92	0.99	0.98	1.00	1.00								
Lu	0.85	0.87	0.96	0.97	0.96	0.97	0.96	0.95	0.98	0.91	0.99	0.99	0.99	0.99	1.00							
Calcite	0.12	0.03	-0.08	-0.08	-0.08	-0.12	-0.06	-0.05	-0.05	0.03	-0.06	-0.06	-0.03	-0.02	0.00	1.00						
Quartz	-0.29	-0.31	-0.46	-0.43	-0.37	-0.36	-0.40	-0.38	-0.35	-0.43	-0.38	-0.42	-0.43	-0.43	-0.47	-0.37	1.00					
Apatite	0.64	0.69	0.75	0.72	0.67	0.63	0.71	0.69	0.66	0.78	0.68	0.67	0.71	0.69	0.73	0.16	-0.55	1.00				
∑Dolomites	0.17	0.22	0.40	0.41	0.39	0.48	0.36	0.34	0.41	0.31	0.43	0.56	0.46	0.48	0.50	-0.12	-0.55	0.47	1.00			
∑Feldspar	-0.41	-0.49	-0.39	-0.41	-0.42	-0.40	-0.41	-0.41	-0.45	-0.44	-0.43	-0.40	-0.40	-0.37	-0.37	0.61	-0.37	-0.06	-0.04	1.00		
Zr	-0.60	-0.61	-0.43	-0.45	-0.48	-0.41	-0.49	-0.51	-0.47	-0.53	-0.44	-0.31	-0.40	-0.40	-0.35	0.22	-0.12	-0.32	-0.06	0.50	1.00	
MnO	0.39	0.46	0.64	0.61	0.55	0.60	0.57	0.54	0.56	0.58	0.59	0.69	0.64	0.63	0.68	0.01	-0.83	0.84	0.77	-0.06	0.07	1.00

If we consider the relations of P_2O_5 contents and the total content of REEs (Figure 43), the Pearson correlation coefficient (R) for limestones is R=0.71, glauconitic sandstones R=0.80, mudstones R=0.59 and phosphorites R=0.63. Calculating the statistical significance (p) with the TTEST function in MS Excel provides p=1.18E-13 for limestones, p=1.86E-33 for glauconitic sandstones, p=4.44E-9 for mudstones, and p=1.98E-14 for phosphorites. Because p<0.05 for all the complexes, there is a statistically significant difference. The highest coefficient of correlation for those variables can be found in the case of glauconitic sandstones (very high correlation), then limestones (high correlation), phosphorites (high correlation), and mudstones (moderate correlation). In all lithologies, the amount of REEs increases with the increase of P_2O_5 content. The similar trends observed suggest that the REE abundance followed the same behaviour in the entire studied section, thus that, even in low proportion, apatite controlled the REE uptake and resulting signals.
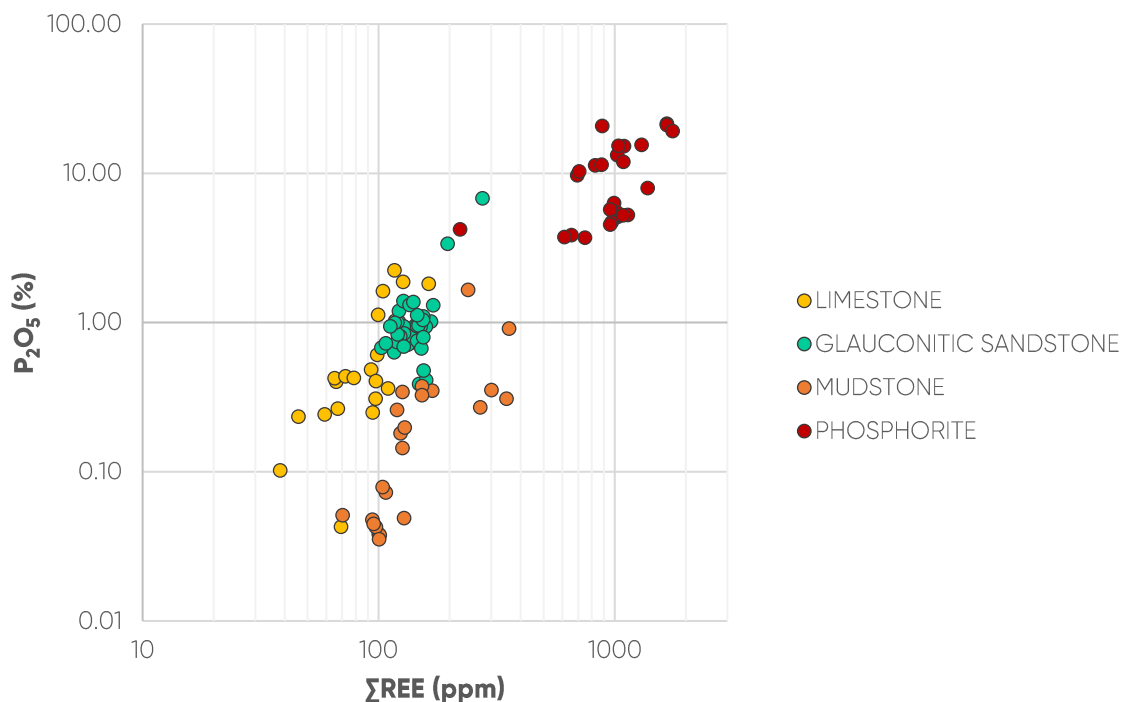

Figure 43. Relation between P_2O_5 and the REEs in all studied rock complexes.

46

As it could be seen from the normalised graphs presented before, there is a significant MREE enrichment in phosphorite samples but also limestones and sandstones, which in general present MREE-enriched patterns with respect to average shales (Bright et al., 2009; Picard et al., 2002), thus confirming the significant influence of apatite on REE signals. Modern seawater exhibits patterns that are enriched in HREE and depleted in LREE, and these patterns have likely remained consistent throughout the Phanerozoic (Shields & Webb, 2004). Consequently, the enrichment of MREE relative to LREE and HREE suggests either a preferential uptake and fractionation relative to seawater or an inheritance from terrigenous sources. Graul, Kallaste, Pajusaar, et al. (2023) interpreted the development of MREE enrichment in shelly phosphorite as a result of progressive uptake and fractionation during diagenesis, influenced by the input of rare earth elements to the primary sediments with Fe-Mn oxyhydroxides.

5.1.3. First Paleoenvironmental Data

To gather more specific insights into sedimentary environments, different **elemental ratios** can deliver valuable clues about the prevailing redox conditions or sources of REEs (Zhao et al., 2021). While neighbouring rare earth elements behave similarly in geological processes, particular environmental conditions might trigger fractionation and decoupling between such REEs, producing distinctive elemental depletion or enrichment in normalised REE patterns. Thus, for example, Ce anomaly, which appears due to the redox-sensitive nature of Ce, is widely used to interpret the paleoredox environment (German & Elderfield, 1990; Gong et al., 2021; Tostevin, 2021). A negative Ce anomaly suggests oxidising conditions, while a positive anomaly is attributed to reducing conditions. The **Ce/Ce* vs Pr/Pr* diagram** (Figure 44) illustrates relationships between Ce and Pr anomalies based on calculated ratios of Equations 2 and 3 (Bau & Dulski, 1996). It is evident from the figure that only shelly phosphorite samples fall into the 'anoxic' field. In contrast, all other samples produce 'suboxic' signatures or reach the 'oxic' ranges for a few limestones.
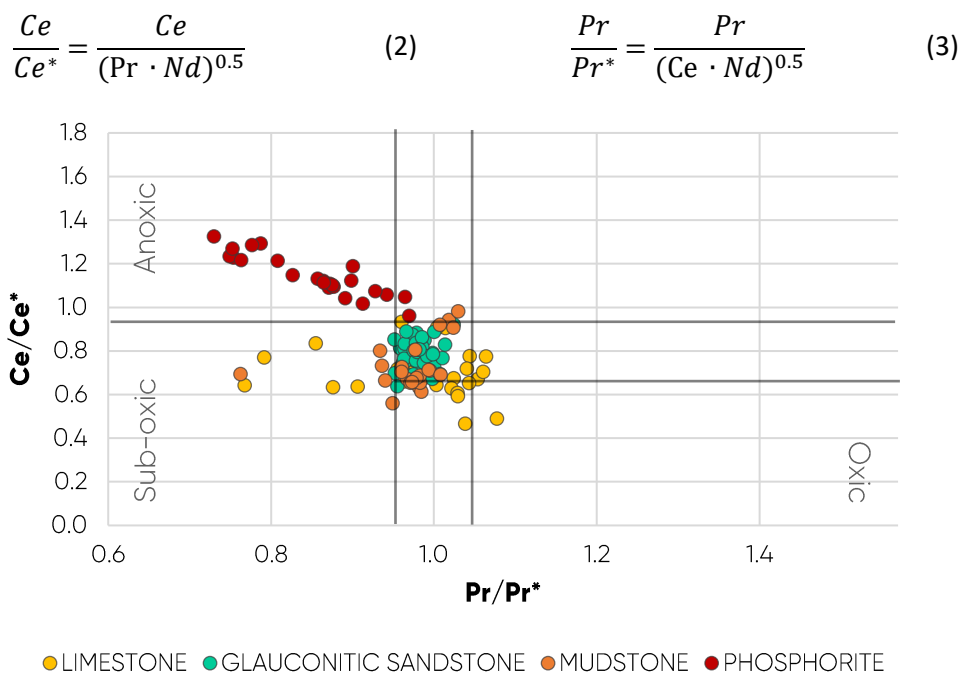
$$\frac{Ce}{Ce^*} = \frac{Ce}{(\mathrm{Pr} \cdot Nd)^{0.5}} \qquad (2) \qquad\qquad \frac{Pr}{Pr^*} = \frac{Pr}{(\mathrm{Ce} \cdot Nd)^{0.5}} \qquad (3)$$

Figure 44. Ce/Ce* vs Pr/Pr* scatter plot. After Bau and Dulski (1996).

To assess whether the sequestered REE budget reflects the inputs of marine or terrigenous sources, the **Y/Ho vs Sm/Yb relations** were investigated (Bau & Dulski, 1996). The Y/Ho variable is employed due to the slightly different properties of these elements: Y is likely to be enriched in oxygen-rich seawater, giving a high Y/Ho ratio in marine settings (Bau & Dulski, 1996; Lumiste et al., 2019). Conversely, in terrigenous sources, Y/Ho tends to be closer to chondrite values (25-30), or even lower based on the detrital sources (Pack et al., 2007). It can be seen in Figure 45, that studied lithologies prevailingly produce a 'terrigenous input' signal, except for phosphorite samples, most of which produce more seawater-like signatures.
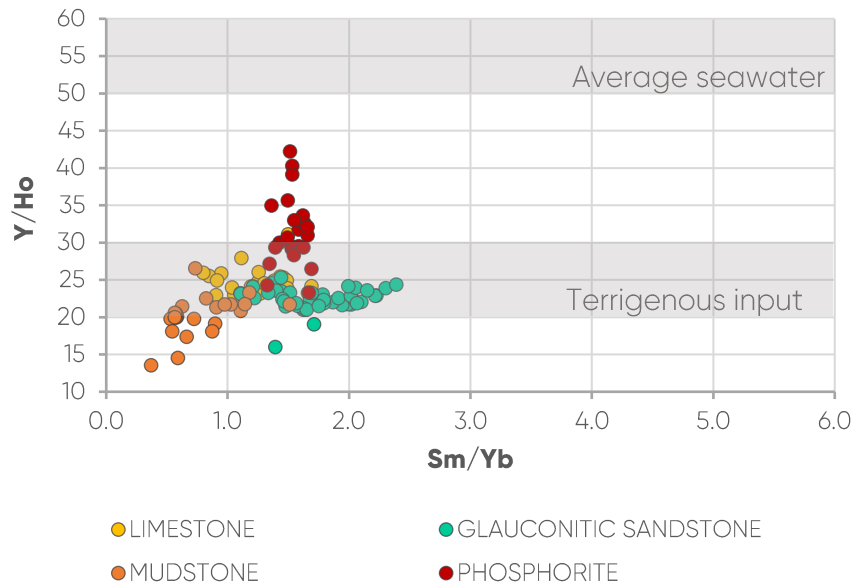
Figure 45. Y/Ho vs Sm/Yb scatter plot. After (Kocsis et al., 2016).

The Eu anomaly observed in the complexes can be derived from multiple sources. To assess the influence of terrigenous mineral vs seawater and the source of Eu anomaly **Ba/Nd vs Eu/Eu* relations** are investigated (Figure 46; Equation 4). The limestone samples produce a high range of Eu/Eu*, however, all the other complexes seem to be grouped. Recorded irregular Eu/Eu* signals for limestone might indicate Ba interferences with Eu signals during ICP-MS measurements leading to overestimation and poor accuracy of Eu values (Barrat et al., 2020). However, this might also indicate a potential hydrothermal influence, as strong positive Eu anomalies have been attributed to high-temperature fluids (Michard & Albarède, 1986); or a Mn and Fe cycling influence in diagenetic environments in the studied limestones (Chen et al., 2023; Hood et al., 2018). Moreover, a few mudstone samples also have higher Eu values. Mudstones are mainly comprised of feldspars, which might dissolve, leading to the remobilisation of related REEs, such as Eu, and redistribution might lead to a local increase of Eu causing an anomaly (Gong et al., 2021).

$$\frac{Eu}{Eu^*} = \frac{Eu}{(Sm \cdot Gd)^{0.5}} \tag{4}$$

Figure 46. Ba/Nd vs Eu/Eu* scatter plot. After (Zhang & Shields, 2023).

The apatite influence also has a pronounced effect on the REE signals. For instance, limestones are likely to have formed in a suboxic t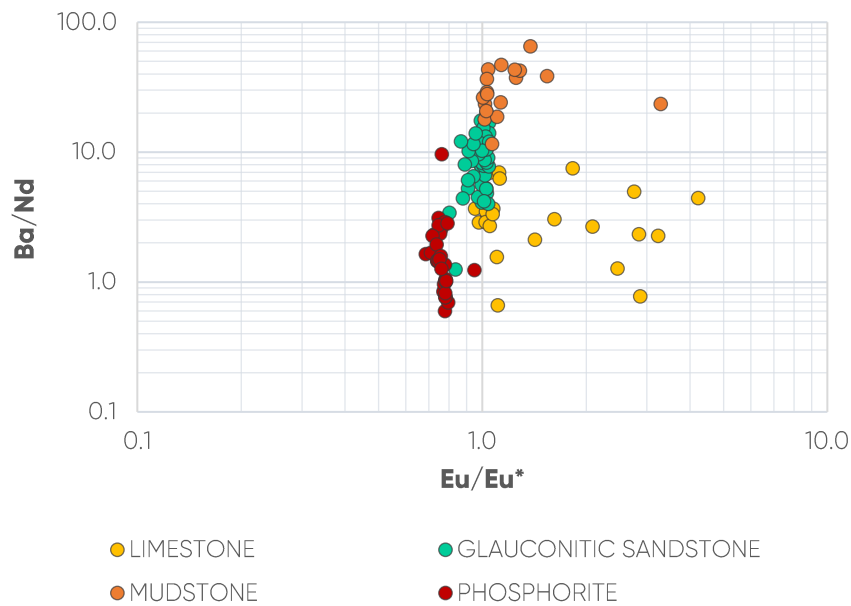o oxic environment (Bau & Dulski, 1996), which is usually indicated by a positive Y anomaly – as observed in Kiipli et al. (2000). Apatite is a mineral that can form during the early diagenesis and 'capture' significant REE content, thus overprinting the other minerals/phases signatures (Lécuyer et al., 2004). The pervasive occurrence of apatite in all complexes indicates that the seawater and sediments were rich in nutrients or organic matter (Gao et al., 2023; Wu et al., 2022).

Glauconitic minerals can be typically found in shallow marine sedimentary environments and are indicative of very slow deposition rates (Rubio & López-Pérez, 2024). The REE content of glauconite is primarily derived from lithogenous clastic material, with minimal contribution from seawater. The commonly observed negative Eu anomaly in glauconite is likely inherited from the source material, which is the substrate on which glauconite's authigenic growth occurred (Tribovillard et al., 2023). Nevertheless, REE signatures for more enriched glauconitic sandstone samples are likely mixed signals obtained due to elevated apatite content.

5.1.4. Limitations and Future Research

Preparing and conducting this thesis was associated with certain limitations. For instance, the scope of sampling was confined to just one borehole, and due to time constraints, many samples still require preparation and analysis to establish full-resolution depth models, particularly for mudstones, where achieving a 1 cm resolution is necessary for paleoenvironmental interpretation. Further research should encompass data from additional sections of the borehole or other boreholes with the same lithologies.

One avenue for exploration could involve developing a regional model for REE distribution in sedimentary deposits to evaluate the regional potential, including neighbouring countries. While the primary objective of this thesis was to provide an overview of the distribution of REEs, the next

step entails utilising the data for more in-depth research and analysis. Additionally, utilising REE proxies to infer past climate and oceanographic conditions could significantly enhance understanding of marine paleoenvironments both from local as well as on a regional perspective. However, interpreting REE data requires expertise in geochemistry, mineralogy, and sedimentology, highlighting the interdisciplinary nature of research in this field. Furthermore, a broader perspective and more detailed background knowledge are essential for conducting further research effectively.

A further aspect, that should be addressed to enhance the investigation of REE signals, is textural analysis, to obtain additional information on mineralogy and trends during diagenesis. In particular, this work would allow to discover the nature of the apatites in the complexes and to study the formation of glauconite.

6. Summary

The study provides the first extensive overview of REEs distribution in Lower Ordovician rock complexes in Estonia including limestones of the Toila Formation, glauconitic sandstone of the Leetse Formation, mudstone of the Varangu Formation, and phosphorite of the Kallavere Formation. The representative data set was composed of 117 whole-rock samples from Aseri PH012B core, which were analysed by multi-instrumental studies to provide mineral, major and trace element composition of the complexes. Obtained results allowed to compose high-resolution depth-tagged models for mineral composition, major components, and REEs distribution providing 5 cm resolution. The created model was investigated along with REE normalised patterns for this study to interpret the REE distribution.

The main average composition of limestone samples analysed confirms the presence of dolomitic limestone with the switch from calcite-dominated lithologies to dolomite-dominated horizons at the lower part of the Toila Formation, with feldspars, muscovite/illite, glauconite and goethite present as minor phases. Glauconitic sandstone presents more complex mineral associations with glauconite, quartz, dolomites, feldspars and muscovite/illite all present as rock-forming phases. Mudstone composition was made of feldspars with quartz and muscovite/illite, which also present as the major phases. The phosphorite is dominated by quartz plus apatite; the content of the latter stays on average near 19%, while pyrite occurs as an important minor phase. The total REE content is on average 95±2 ppm for limestones, 142±2 ppm for glauconitic sandstones, 157±6 ppm for mudstones and 1026±23 ppm for phosphorites.

The shale normalised REE patterns of the studied complexes suggest that the enrichment levels of these complexes are similar to that of average shale. However, in the case of phosphorite, some REEs show up to ten-fold enrichment with respect to reference values. Limestone samples exhibit a pronounced negative Ce anomaly and a strong positive Eu anomaly; glauconitic sandstone samples show a strong negative anomaly for Ce and Y; mudstone samples display strong positive Eu peaks in certain instances; and some phosphorite samples present a negative anomaly for Ce and Y. Despite the varying enrichment levels, a common feature of the limestones, glauconitic sandstones, and phosphorite is MREE enrichment.

Correlation analyses between REE and other compounds in the studied limestones show a strong positive correlation between most of the REEs, except for Eu and La, and medium or weak correlation with other elements. The lack of covariance with calcite indicates that calcite formation did not have primary control on REE accumulation in the sediments. The measured REE signal is likely partly inherited from terrigenous fraction. Regarding glauconitic sandstones, there is a strong positive correlation between most REEs, except La, which shows a low covariance with other REEs. None to strong negative correlation was detected between glauconite and all REEs. Notably strong to very strong positive correlation between apatite and REEs was detected, suggesting the REE capture in glauconitic sandstones is most likely connected to apatite distribution. For mudstones, a strong positive correlation between all REEs, except La which had a weaker correlation with others, was observed. REEs show a moderately strong correlation with apatite and quartz, except Eu, which presents weak covariance with apatite distribution. Considering that the REE enrichment is statistically connected to quartz and apatite, apatite is likely the main carrier phase of REEs. A strong

positive correlation in phosphorites can be detected with all the REE-s except with La and Ce, which show slightly lower correlation coefficient values. The strongest correlation of REEs with other compounds appears with apatite, dolomites and MnO. Consequently, the enrichment of MREE relative to LREE and HREE suggests a preferential uptake and fractionation relative to seawater.

To gather more specific insights into sedimentary environments, different elemental ratios were delivered to gain clues about the prevailing redox conditions or sources of REEs. The Ce/Ce* vs Pr/Pr* diagram showed, that only shelly phosphorite samples fall into the 'anoxic' field, while all other samples produce 'suboxic' signatures or for a few limestones, reach the 'oxic' ranges. To assess whether the sequestered REE budget reflects the inputs of marine or terrigenous sources, the Y/Ho vs Sm/Yb relations were investigated. It was concluded that studied lithologies prevailingly produce a 'terrigenous input' signal, except for phosphorite samples, most of which produce more seawater-like signatures. To further assess the influence of terrigenous mineral vs seawater Ba/Nd vs Eu/Eu* relations were investigated. The limestone and mudstone samples produced a higher range of Eu/Eu* values; however, all the other complexes clustered into one group. Recorded irregular Eu/Eu* signals for limestones and mudstones might indicate Ba interferences with Eu signals during ICP-MS measurements leading to overestimation and poor accuracy of Eu values. However, one can't exclude a potential hydrothermal or a Mn and Fe cycling influence in a diagenetic environment as a potential source for Eu anomaly.

As mentioned, this is the first systematic high-resolution study on REE variability in Estonian Lower Palaeozoic complexes using whole rock data of different lithologies. As a part of this thesis, a general overview of the REE distribution in selected complexes has been provided, and some possible reasoning behind the results has been discussed. The data of this thesis will be published later together with additional data from black shale and mudstone intervals in case of what 1 cm resolution is aimed. Regarding future research, the scope of sampling for this thesis was confined to just one borehole. Further research should encompass data from additional sections of the borehole or other boreholes from the same lithologies. The next step also entails utilising the data for more in-depth research to infer past climate and oceanographic conditions and to enhance REE deposit models.

7. Acknowledgements

I would like to express my deepest gratitude to my thesis supervisors, Rutt Hints and Sophie Graul. From the very beginning, it has been a joy working under your supervision. I am grateful for your support throughout this entire journey. You provided more than enough assistance, from the initial preparation activities to guidance on the thesis and help with sample preparation in the lab. Your invaluable guidance and exceptional attention to detail have been outstanding, and I have learned a great deal both in knowledge and skills during this process.

Furthermore, thank you for sharing your experience and knowledge, providing background information, and offering profound expertise on related topics. While there is still much I don't know about the subject, this is the nature of science, where new discoveries are made every day. Collaborating with you has been truly inspiring and has undoubtedly enriched the final year of my master's studies.

Also, thank you for your trust and for believing in me. Many thanks for your dedication and for investing your valuable time into the entire process. Although I wish I had started the thesis preparation even earlier and not left much of the writing until the final stages, I remind myself that 'diamonds are made under pressure'. Thank you for helping to shape this diamond and for your patience, answering my emails early in the morning, late at night, and even on weekends when needed. And Sophie, I'm genuinely grateful for your late-night *motivational kalad* and for maintaining a positive spirit every step of the way.

I would also like to thank Nata-Ly Pantšenko and Toivo Kallaste for your help, guidance and mentoring with sample preparation and interpretation in the laboratory, as well as Andre Gregor, for running ICP-MS samples.

8. References

Abbott, A. N., Löhr, S., & Trethewy, M. (2019). Are Clay Minerals the Primary Control on the Oceanic Rare Earth Element Budget? [Original Research]. *Frontiers in Marine Science*, *6*. https://doi.org/10.3389/fmars.2019.00504

Agilent Technologies, I. (2024). *An Introduction to the Fundamentals of Inductively Coupled Plasma – Mass Spectrometry (ICP-MS)*. Retrieved 26.05 from https://www.agilent.com/en/product/atomic-spectroscopy/inductively-coupled-plasma-mass-spectrometry-icp-ms/what-is-icp-ms-icp-ms-faqs

Auer, G., Reuter, M., Hauzenberger, C. A., & Piller, W. E. (2017). The impact of transport processes on rare earth element patterns in marine authigenic and biogenic phosphates. *Geochimica et Cosmochimica Acta*, *203*, 140-156. https://doi.org/https://doi.org/10.1016/j.gca.2017.01.001

Barrat, J.-A., Bayon, G., Wang, X., Le Goff, S., Rouget, M.-L., Gueguen, B., & Ben Salem, D. (2020). A new chemical separation procedure for the determination of rare earth elements and yttrium abundances in carbonates by ICP-MS. *Talanta*, *219*, 121244. https://doi.org/https://doi.org/10.1016/j.talanta.2020.121244

Bau, M., & Dulski, P. (1996). Distribution of yttrium and rare-earth elements in the Penge and Kuruman iron-formations, Transvaal Supergroup, South Africa. *Precambrian Research*, *79*(1), 37-55. https://doi.org/https://doi.org/10.1016/0301-9268(95)00087-9

Bayon, G., Toucanne, S., Skonieczny, C., André, L., Bermell, S., Cheron, S., Dennielou, B., Etoubleau, J., Freslon, N., Gauchery, T., Germain, Y., Jorry, S. J., Ménot, G., Monin, L., Ponzevera, E., Rouget, M. L., Tachikawa, K., & Barrat, J. A. (2015). Rare earth elements and neodymium isotopes in world river sediments revisited. *Geochimica et Cosmochimica Acta*, *170*, 17-38. https://doi.org/https://doi.org/10.1016/j.gca.2015.08.001

Bright, C. A., Cruse, A. M., Lyons, T. W., MacLeod, K. G., Glascock, M. D., & Ethington, R. L. (2009). Seawater rare-earth element patterns preserved in apatite of Pennsylvanian conodonts? *Geochimica et Cosmochimica Acta*, *73*(6), 1609-1624. https://doi.org/https://doi.org/10.1016/j.gca.2008.12.014

Bright, J. (2020). *Investigating the use of a positive Europium anomaly and marine Y/Ho ratios as potential fingerprints for Gulf of California hydrochemistry with implications for the origin of southern Bouse Formation carbonate (Arizona and California, USA)*.

British Geological Survey. (2011). *Rare Earth Elements*.

Bruker. (2024). *How does XRF Work?* Retrieved 26.05 from https://www.bruker.com/en/products-and-solutions/elemental-analyzers/xrf-spectrometers/how-does-xrf-work.html

Chen, F., Wang, Q., Pufahl, P. K., Matheson, E. J., Xian, H., Nan, J., Ma, H., & Deng, J. (2023). Carbonate-hosted manganese deposits and ocean anoxia. *Earth and Planetary Science Letters*, *622*, 118385. https://doi.org/https://doi.org/10.1016/j.epsl.2023.118385

Dutta, T., Kim, K.-H., Uchimiya, M., Kwon, E. E., Jeon, B.-H., Deep, A., & Yun, S.-T. (2016). Global demand for rare earth resources and strategies for green mining. *Environmental Research*, *150*, 182-190. https://doi.org/https://doi.org/10.1016/j.envres.2016.05.052

Elkina, V., & Kurushkin, M. (2020). Promethium: To Strive, to Seek, to Find and Not to Yield [Mini Review]. *Frontiers in Chemistry*, *8*. https://doi.org/10.3389/fchem.2020.00588

eMaapõu. (2024). *Aseri PH012B borehole*. Retrieved 13.05 from https://geoloogia.info/en/locality/23777/drillcore-boxes

Estonian Land Board. (2024). *X-GIS Map*. Retrieved 13.04.2024 from https://xgis.maaamet.ee/xgis2/page/app/core_aluskaardid

European Commission. (2023). *Critical raw materials*. Retrieved 25.05 from https://single-market-economy.ec.europa.eu/sectors/raw-materials/areas-specific-interest/critical-raw-

materials_en#:~:text=The%202020%20criticality%20assessment%20was,to%2083%20mat
erials%20in%20total).

Gao, L., Yang, R., Wu, T., Luo, C., Xu, H., & Ni, X. (2023). Studies on geochemical characteristics and biomineralization of Cambrian phosphorites, Zhijin, Guizhou Province, China. *PLOS ONE*, *18*(2), e0281671. https://doi.org/10.1371/journal.pone.0281671

German, C. R., & Elderfield, H. (1990). Application of the Ce anomaly as a paleoredox indicator: The ground rules. *Palaeogeography*, *5*(5), 823-833. https://doi.org/https://doi.org/10.1029/PA005i005p00823

Gong, Q., Li, F., Lu, C., Wang, H., & Tang, H. (2021). Tracing seawater- and terrestrial-sourced REE signatures in detritally contaminated, diagenetically altered carbonate rocks. *Chemical Geology*, *570*, 120169. https://doi.org/10.1016/j.chemgeo.2021.120169

Graul, S., Kallaste, T., Moilanen, M., Monchal, V., Ndiaye, M., & Hints, R. (2023). Early diagenetic transformation stages revealed by micro-analytical studies of shelly phosphorites, Rakvere region. *Estonian Journal of Earth Sciences*, *72*, 34. https://doi.org/10.3176/earth.2023.12

Graul, S., Kallaste, T., Pajusaar, S., Urston, K., Gregor, A., Moilanen, M., Ndiaye, M., & Hints, R. (2023). REE + Y distribution in Tremadocian shelly phosphorites (Toolse, Estonia): Multi-stages enrichment in shallow marine sediments during early diagenesis. *Journal of Geochemical Exploration*, *254*, 107311. https://doi.org/https://doi.org/10.1016/j.gexplo.2023.107311

Grenier, M., Garcia-Solsona, E., Lemaitre, N., Trull, T. W., Bouvier, V., Nonnotte, P., van Beek, P., Souhaut, M., Lacan, F., & Jeandel, C. (2018). Differentiating Lithogenic Supplies, Water Mass Transport, and Biological Processes On and Off the Kerguelen Plateau Using Rare Earth Element Concentrations and Neodymium Isotopic Compositions [Original Research]. *Frontiers in Marine Science*, *5*. https://doi.org/10.3389/fmars.2018.00426

Harkins, W. D. (1917). The Evolution of the Elements and the Stability of Complex Atoms. I. A New Periodic System Which Shows a Relation Between the Abundance of the Elements and the Structure of the Nuclei of Atoms. *Journal of the American Chemical Society*, *39*(5), 856-879. https://doi.org/10.1021/ja02250a002

Harper, D. A. T., Lefebvre, B., Percival, I. G., & Servais, T. (2023). *A Global Synthesis of the Ordovician System*. Geological Society. https://books.google.ee/books?id=z6IK0AEACAAJ

Hood, A. v. S., Planavsky, N. J., Wallace, M. W., & Wang, X. (2018). The effects of diagenesis on geochemical paleoredox proxies in sedimentary carbonates. *Geochimica et Cosmochimica Acta*, *232*, 265-287. https://doi.org/https://doi.org/10.1016/j.gca.2018.04.022

Jaireth, S., Hoatson, D. M., & Miezitis, Y. (2014). Geological setting and resources of the major rare-earth-element deposits in Australia. *Ore Geology Reviews*, *62*, 72-128. https://doi.org/https://doi.org/10.1016/j.oregeorev.2014.02.008

Kechiched, R., Laouar, R., Bruguier, O., Salmi-Laouar, S., Kocsis, L., Bosch, D., Foufou, A., Ameur-Zaimeche, O., & Larit, H. (2018). Glauconite-bearing sedimentary phosphorites from the Tébessa region (eastern Algeria): Evidence of REE enrichment and geochemical constraints on their origin. *Journal of African Earth Sciences*, *145*, 190-200. https://doi.org/https://doi.org/10.1016/j.jafrearsci.2018.05.018

Khan, H., Yerramilli, A. S., D'Oliveira, A., Alford, T. L., Boffito, D. C., & Patience, G. S. (2020). Experimental methods in chemical engineering: X-ray diffraction spectroscopy—XRD. *The Canadian Journal of Chemical Engineering*, *98*(6), 1255-1266. https://doi.org/https://doi.org/10.1002/cjce.23747

Kiipli, T., Batchelor, R., J.P, B., Cowing, C., Hagel-Brunnstrom, M., Ingham, M., Johnson, D., Kivisilla, J., Knaack, C., Kump, P., Lozano-Santacruz, R., Michiels, D., Orlova, K., Pirrus, E., Rousseau, R., Ruzicka, J., Sandstrom, H., & Willis, J. (2000). Seven sedimentary rock reference samples from Estonia. *Oil Shale*, *17*, 215-223. https://doi.org/10.3176/oil.2000.3.02

Kocsis, L., Gheerbrant, E., Mouflih, M., Cappetta, H., Ulianov, A., Chiaradia, M., & Bardet, N. (2016). Gradual changes in upwelled seawater conditions (redox, pH) from the late Cretaceous through early Paleogene at the northwest coast of Africa: Negative Ce anomaly trend recorded in fossil bio-apatite. *Chemical Geology*, *421*, 44-54. https://doi.org/https://doi.org/10.1016/j.chemgeo.2015.12.001

Lécuyer, C., Reynard, B., & Grandjean, P. (2004). Rare earth element evolution of Phanerozoic seawater recorded in biogenic apatites. *Chemical Geology*, *204*(1), 63-102. https://doi.org/https://doi.org/10.1016/j.chemgeo.2003.11.003

Lumiste, K., Lang, L., Paiste, P., Lepland, A., & Kirsimäe, K. (2021). Heterogeneous REE + Y distribution in Early Paleozoic shelly phosphorites: Implications for enrichment mechanisms. *Chemical Geology*, *586*, 120590. https://doi.org/https://doi.org/10.1016/j.chemgeo.2021.120590

Lumiste, K., Mänd, K., Bailey, J., Paiste, P., Lang, L., Lepland, A., & Kirsimäe, K. (2019). REE+Y uptake and diagenesis in Recent sedimentary apatites. *Chemical Geology*, *525*, 268-281. https://doi.org/https://doi.org/10.1016/j.chemgeo.2019.07.034

Makonnen, Y., & Beauchemin, D. (2020). Chapter 1 - The inductively coupled plasma as a source for optical emission spectrometry and mass spectrometry. In D. Beauchemin (Ed.), *Sample Introduction Systems in ICPMS and ICPOES* (pp. 1-55). Elsevier. https://doi.org/https://doi.org/10.1016/B978-0-444-59482-2.00001-4

Malvern Panalytical Ltd. (2024). *X-ray Diffraction (XRD)*. Retrieved 26.05 from https://www.malvernpanalytical.com/en/products/technology/xray-analysis/x-ray-diffraction#:~:text=X%2Dray%20diffraction%20(XRD)%20is%20a%20versatile%20non%2D,made%20up%20of%20tiny%20crystallites.

Marguí, E., Queralt, I., & de Almeida, E. (2022). X-ray fluorescence spectrometry for environmental analysis: Basic principles, instrumentation, applications and recent trends. *Chemosphere*, *303*, 135006. https://doi.org/https://doi.org/10.1016/j.chemosphere.2022.135006

Meermann, B., & Nischwitz, V. (2018). ICP-MS for the analysis at the nanoscale – a tutorial review [10.1039/C8JA00037A]. *Journal of Analytical Atomic Spectrometry*, *33*(9), 1432-1468. https://doi.org/10.1039/C8JA00037A

Meidla, T. (2020). Cambrian stratigraphic chart of Estonia. Estonian Commission on Stratigraphy. In: Estonian Commission on Stratigraphy.

Meidla, T., Ainsaar, L., & Hints, O. (2014). The Ordovician System in Estonia. In *4th Annual Meeting of IGCP 591 The Early to Middle Paleozoic Revolution Estonia* (pp. 116-122).

Meidla, T., Ainsaar, L., Hints, O., & Radzevičius, S. (2023). Ordovician of the Eastern Baltic palaeobasin and the Tornquist Sea margin of Baltica. *Geological Society, London, Special Publications*, *532*(1), 317-343. https://doi.org/10.1144/SP532-2022-141

Michard, A., & Albarède, F. (1986). The REE content of some hydrothermal fluids. *Chemical Geology*, *55*(1), 51-60. https://doi.org/https://doi.org/10.1016/0009-2541(86)90127-0

Ndiaye, M., Liiv, M., Kallaste, T., Graul, S., & Hints, R. (2023). Nitrogen and organic carbon isotope record in Tremadocian highly metalliferous black shales from Baltica. *Estonian Journal of Earth Sciences*, *72*(1), 78-81. https://doi.org/https://doi.org/10.3176/earth.2023.25

Ndiaye, M., Pajusaar, S., Liiv, M., Graul, S., Kallaste, T., & Hints, R. (2023). Fine clay shuttle as a key mechanism for V hyper-enrichment in shallow water Tremadocian black shale from Baltica. *Chemical Geology*, *634*, 121583. https://doi.org/https://doi.org/10.1016/j.chemgeo.2023.121583

Nestor, H., Soesoo, A., Linna, A., Hints, O., & Nõlvak, J. (2007). *The Ordovician in Estonia and Southern Finland*.

Nielsen, A., Schovsbo, N., Klitten, K., Woollhead, D., & Rasmussen, C. (2018). Gamma-ray log correlation and stratigraphic architecture of the Cambro-Ordovician Alum Shale

Formation on Bornholm, Denmark: Evidence for differential syndepositional isostasy. *Bulletin of the Geological Society of Denmark*, *66*, 237-273. https://doi.org/10.37570/bgsd-2018-66-15

Oyedotun, T. D. T. (2018). X-ray fluorescence (XRF) in the investigation of the composition of earth materials: a review and an overview. *Geology, Ecology, and Landscapes*, *2*(2), 148-154. https://doi.org/10.1080/24749508.2018.1452459

Pack, A., Russell, S. S., Shelley, J. M. G., & van Zuilen, M. (2007). Geo- and cosmochemistry of the twin elements yttrium and holmium. *Geochimica et Cosmochimica Acta*, *71*(18), 4592-4608. https://doi.org/https://doi.org/10.1016/j.gca.2007.07.010

Picard, S., Lécuyer, C., Barrat, J.-A., Garcia, J.-P., Dromart, G., & Sheppard, S. M. F. (2002). Rare earth element contents of Jurassic fish and reptile teeth and their potential relation to seawater composition (Anglo-Paris Basin, France and England). *Chemical Geology*, *186*(1), 1-16. https://doi.org/https://doi.org/10.1016/S0009-2541(01)00424-7

Potts, P. J. (1987). X-ray fluorescence analysis: principles and practice of wavelength dispersive spectrometry. In P. J. Potts (Ed.), *A Handbook of Silicate Rock Analysis* (pp. 226-285). Springer Netherlands. https://doi.org/10.1007/978-94-015-3988-3_8

Raukas, A., & Teedumäe, A. (1997). *Geology and Mineral Resources of Estonia*. Estonian Academy Publishers. https://books.google.ee/books?id=ULmSQAAACAAJ

Rubio, B., & López-Pérez, A. E. (2024). Exploring the genesis of glauncony and verdine facies for paleoenvironmental interpretation: A review. *Sedimentary Geology*, *461*, 106579. https://doi.org/https://doi.org/10.1016/j.sedgeo.2024.106579

Saltzman, M. R., Young, S. A., Kump, L. R., Gill, B. C., Lyons, T. W., & Runnegar, B. (2011). Pulse of atmospheric oxygen during the late Cambrian. *Proceedings of the National Academy of Sciences*, *108*(10), 3876-3881. https://doi.org/10.1073/pnas.1011836108

Schramm, R. (2016). Use of X-ray Fluorescence Analysis for the Determination of Rare Earth Elements. *1*(9). https://doi.org/doi:10.1515/psr-2016-0061 (Physical Sciences Reviews)

Shields, G., & Stille, P. (2001). Diagenetic constraints on the use of cerium anomalies as palaeoseawater redox proxies: an isotopic and REE study of Cambrian phosphorites. *Chemical Geology*, *175*(1), 29-48. https://doi.org/https://doi.org/10.1016/S0009-2541(00)00362-4

Shields, G. A., & Webb, G. E. (2004). Has the REE composition of seawater changed over geological time? *Chemical Geology*, *204*(1), 103-107. https://doi.org/https://doi.org/10.1016/j.chemgeo.2003.09.010

Sholkovitz, E. R. (1990). Rare-earth elements in marine sediments and geochemical standards. *Chemical Geology*, *88*(3), 333-347. https://doi.org/https://doi.org/10.1016/0009-2541(90)90097-Q

Soesoo, A. (2022). *Critical Earth Resources: an Estonian Contribution*.

Speakman, S. A. (2011). Basics of X-ray powder diffraction. In: MIT Center for Materials Science and Engineering.

Tadayon, Y., Vantelon, D., Gigault, J., Dia, A., Pattier, M., Dutruch, L., & Davranche, M. (2024). Rare earth elements interaction with iron-organic matter colloids as a control of the REE environmental dissemination. *Journal of Colloid and Interface Science*, *655*, 70-79. https://doi.org/https://doi.org/10.1016/j.jcis.2023.10.110

Taylor, S. R., & McLennan, S. M. (1985). The Continental Crust: Its Composition and Evolution. *Geological Magazine*, *122*(6), 673-674. https://doi.org/10.1017/S0016756800032167

ThermoFisher. (2020). *What is XRF (X-ray Fluorescence) and How Does it Work?* Retrieved 26.05 from https://www.thermofisher.com/blog/ask-a-scientist/what-is-xrf-x-ray-fluorescence-and-how-does-it-work/

Thomas, R. (2001). A Beginner's Guide to ICP-MS. *Spectroscopy*, *16*(4). http://scientificsolutions1.com/Beginners%20guide%20to%20ICP-MS.pdf

Tostevin, R. (2021). *Cerium Anomalies and Paleoredox*. https://doi.org/10.1017/9781108847223

Tostevin, R., Shields, G. A., Tarbuck, G. M., He, T., Clarkson, M. O., & Wood, R. A. (2016). Effective use of cerium anomalies as a redox proxy in carbonate-dominated marine settings. *Chemical Geology*, *438*, 146-162. https://doi.org/https://doi.org/10.1016/j.chemgeo.2016.06.027

Tribovillard, N., Bout-Roumazeilles, V., Abraham, R., Ventalon, S., Delattre, M., & Baudin, F. (2023). The contrasting origins of glauconite in the shallow marine environment highlight this mineral as a marker of paleoenvironmental conditions. *Comptes Rendus. Géoscience*, *355*(S2), 213-228. https://doi.org/10.5802/crgeos.170

Trotter, J., Williams, I., Barnes, C., Lécuyer, C., & Nicoll, R. (2008). Did Cooling Oceans Trigger Ordovician Biodiversification? Evidence from Conodont Thermometry. *Science (New York, N.Y.)*, *321*, 550-554. https://doi.org/10.1126/science.1155814

Van Gosen, B. S., Verplanck, P. L., Seal Ii, R. R., Long, K. R., & Gambogi, J. (2017). *Rare-Earth Elements* [Report](1802O). (Professional Paper, Issue. U. S. G. Survey. https://pubs.usgs.gov/publication/pp1802O

Voolma, M., Soesoo, A., Hade, S., Hints, R., & Toivo, K. (2013). Geochemical heterogeneity of Estonian graptolite argillite. *Oil Shale*, *30*, 377-401. https://doi.org/10.3176/oil.2013.3.02

Wu, S., Yang, H., Fan, H., Xia, Y., Meng, Q., He, S., & Gong, X. (2022). Assessment of the Effect of Organic Matter on Rare Earth Elements and Yttrium Using the Zhijin Early Cambrian Phosphorite as an Example. *Minerals*, *12*(7).

Yang, L. (2009). Accurate and precise determination of isotopic ratios by MC-ICP-MS: A review. *Mass Spectrometry Reviews*, *28*(6), 990-1011. https://doi.org/https://doi.org/10.1002/mas.20251

Zhang, K., & Shields, G. A. (2023). Early diagenetic mobilization of rare earth elements and implications for the Ce anomaly as a redox proxy. *Chemical Geology*, *635*, 121619. https://doi.org/https://doi.org/10.1016/j.chemgeo.2023.121619

Zhao, Y., Wei, W., Li, S., Yang, T., Zhang, R., Somerville, I., Santosh, M., Wei, H., Wu, J., Yang, J., Chen, W., & Tang, Z. (2021). Rare earth element geochemistry of carbonates as a proxy for deep-time environmental reconstruction. *Palaeogeography, Palaeoclimatology, Palaeoecology*, *574*, 110443. https://doi.org/https://doi.org/10.1016/j.palaeo.2021.110443

Zhou, B., Li, Z., & Chen, C. (2017). Global Potential of Rare Earth Resources and Rare Earth Demand from Clean Technologies. *Minerals*, *7*(11).

Appendices

Appendix 1. PH012B Sample Description and REE Distribution
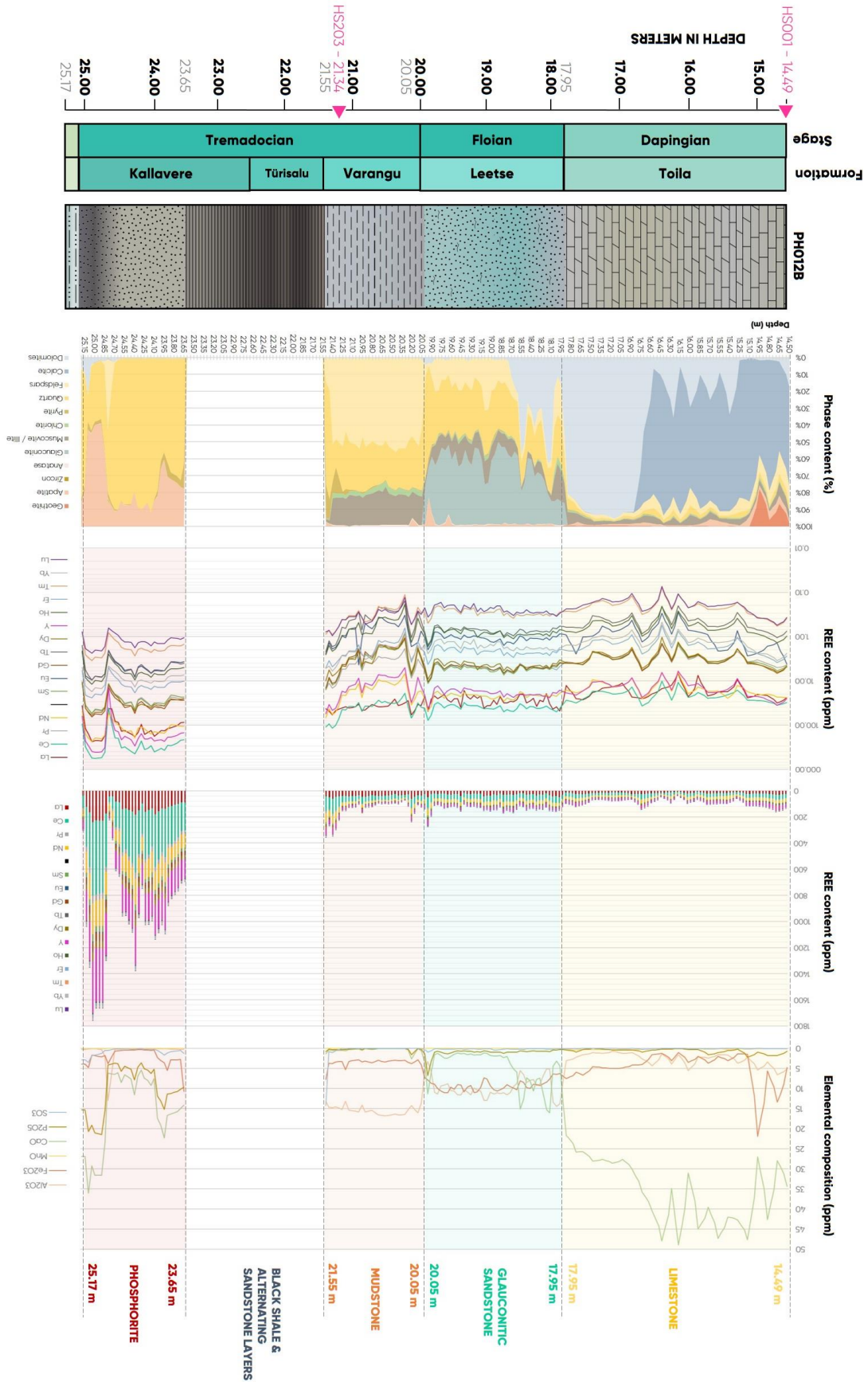
Non-exclusive licence for reproduction and publication of a graduation thesis

I Henri Olavi Suomalainen,

1. grant Tallinn University of Technology free licence (non-exclusive licence) for my thesis
Distribution of Rare Earth Elements in Estonian Lower Ordovician Complexes,

supervised by Rutt Hints & Sophie Graul,

1.1 to be reproduced for the purposes of preservation and electronic publication of the graduation thesis, incl. to be entered in the digital collection of the library of Tallinn University of Technology until expiry of the term of copyright;

1.2 to be published via the web of Tallinn University of Technology, incl. to be entered in the digital collection of the library of Tallinn University of Technology until expiry of the term of copyright.

2. I am aware that the author also retains the rights specified in clause 1 of the non-exclusive licence.

3. I confirm that granting the non-exclusive licence does not infringe other persons' intellectual property rights, the rights arising from the Personal Data Protection Act or rights arising from other legislation.

(Digitally signed)

---

[1] *The non-exclusive licence is not valid during the validity of access restriction indicated in the student's application for restriction on access to the graduation thesis that has been signed by the school's dean, except in case of the university's right to reproduce the thesis for preservation purposes only. If a graduation thesis is based on the joint creative activity of two or more persons and the co-author(s) has/have not granted, by the set deadline, the student defending his/her graduation thesis consent to reproduce and publish the graduation thesis in compliance with clauses 1.1 and 1.2 of the non-exclusive licence, the non-exclusive license shall not be valid for the period.*